A&A 604, A43 (2017)
DOI: 10.1051/0004-6361/201730563

Astronomy & Astrophysics

Kinematics and physical conditions of H I in nearby radio sources

The last survey of the old Westerbork Synthesis Radio Telescope

F. M. Maccagni[1,2], R. Morganti[1,2], T. A. Oosterloo[1,2], K. Geréb[3], and N. Maddox[2]

[1] Kapteyn Astronomical Institute, University of Groningen, Postbus 800, 9700 AV Groningen, The Netherlands
[2] ASTRON, Netherlands Institute for Radio Astronomy, Postbus 2, 7990 AA Dwingeloo, The Netherlands
[3] Centre for Astrophysics and Supercomputing, Swinburne University of Technology, Hawthorn, 3122 Victoria, Australia
e-mail: maccagni@astro.rug.nl

Received 5 February 2017 / Accepted 17 April 2017

ABSTRACT

We present an analysis of the properties of neutral hydrogen (H I) in 248 nearby ($0.02 < z < 0.25$) radio galaxies with $S_{1.4\,\mathrm{GHz}} > 30$ mJy and for which optical spectroscopy is available. The observations were carried out with the Westerbork Synthesis Radio Telescope as the last large project before the upgrade of the telescope with phased array feed receivers (Apertif). The sample covers almost four orders of magnitude in radio power from $\log P_{1.4\,\mathrm{GHz}} = 22.5$ W Hz^{-1} and 26.2 W Hz^{-1}. We detect H I in absorption in 27% ± 5.5% of the objects. The detections are found over the full range of radio power. However, the distribution and kinematics of the absorbing H I gas appear to depend on radio power, the properties of the radio continuum emission, and the dust content of the sources. Among the sources where H I is detected, gas with kinematics deviating from regular rotation is more likely found as the radio power increases. In the great majority of these cases, the H I profile is asymmetric with a significant blue-shifted component. This is particularly common for sources with $\log P_{1.4\,\mathrm{GHz}} > 24$ W Hz^{-1}, where the radio emission is small, possibly because these radio sources are young. The same is found for sources that are bright in the mid-infrared, i.e. sources rich in heated dust. In these sources, the H I is outflowing likely under the effect of the interaction with the radio emission. Conversely, in dust-poor galaxies, and in sources with extended radio emission, at all radio powers we only detect H I distributed in a rotating disk. Stacking experiments show that in sources for which we do not detect H I in absorption directly, the H I has a column density that is lower than $3.5 \times 10^{17}\,(T_{\mathrm{spin}}/c_f)$ cm^{-2}. We use our results to predict the number and type of H I absorption lines that will be detected by the upcoming surveys of the Square Kilometre Array precursors and pathfinders (Apertif, MeerKAT, and ASKAP).

Key words. radio lines: ISM – radio lines: galaxies – galaxies: nuclei – galaxies: ISM – infrared: ISM

1. Introduction

The interaction between the energy released by the active central supermassive black hole (SMBH) and the surrounding interstellar medium (ISM) plays an important role in galaxy evolution. This interaction affects the star formation history of the host galaxy and the observed relation between the masses of the bulge and central black hole (e.g. Silk & Rees 1998, Bower et al. 2006; Ciotti et al. 2010; Faucher-Giguère & Quataert 2012; Faucher-Giguere et al. 2013; King & Pounds 2015; King & Nixon 2015).

The actual effect of this interplay depends on the properties of the ISM and the type of active galactic nucleus (AGN) in the host galaxy. Among the diverse families of active AGN, radio AGN show radio jets expanding through the ISM. This facilitates a detailed study of the effects of the nuclear activity on the kinematics of the different components of the gas, i.e. the ionised gas (e.g. Tadhunter et al. 2000; Holt et al. 2003; McNamara & Nulsen 2007; Holt et al. 2008; Labiano 2008; Reeves et al. 2009; Fabian 2012), the molecular gas (e.g. García-Burillo et al. 2005; Feruglio et al. 2010; Alatalo et al. 2011; Dasyra & Combes 2011; Guillard et al. 2012; Morganti et al. 2013b, 2015, 2016; Mahony et al. 2016; Maccagni et al. 2016) and the atomic gas (e.g. Morganti et al. 2005a,b, 2013a; Lehnert et al. 2011; Allison et al. 2015). In radio AGN it is possible to estimate the age of the activity directly from the peaked radio continuum spectrum and from the extent and expansion velocity of its radio jets. Hence, it is possible to study the effects of the nuclear activity on the ISM at different stages of its evolution.

Observations of the neutral hydrogen (H I) in early-type galaxies, which are the typical hosts of a radio AGN, allow us to study the cold gas in relation to their star formation and nuclear activity. A number of studies (e.g. Morganti et al. 2006; Oosterloo et al. 2010a; Emonts et al. 2010; Serra et al. 2012, 2014) show that a significant fraction of early-type galaxies (∼40%) have H I detected in emission, which can be found in settled rotating disks and in unsettled configurations. The H I may represent the reservoir of cold gas for the formation of new stars in early-type galaxies, and, likely, also for the fuelling of the central SMBH. When the AGN are radio loud, H I seen against the radio continuum has been used to study the morphology and kinematics of the cold gas in their very centre (e.g. van Gorkom et al. 1989; Morganti et al. 2001, 2005b; Vermeulen et al. 2003; Gupta et al. 2006). H I absorption lines can trace a wide variety of morphologies and phenomena. In some radio AGN, the detection of H I in emission and absorption has allowed us to associate the H I absorption lines detected at the systemic velocity of the galaxy with a circumnuclear rotating disk (e.g. van der Hulst et al. 1983; Conway & Blanco 1995; Beswick et al. 2002, 2004; Struve & Conway 2010; Struve et al. 2010). Narrow ($\lesssim$50 km s^{-1}) H I absorption lines offset with respect to the systemic velocity have been in

some cases associated with the fuelling of the radio sources (e.g. Morganti et al. 2009; Maccagni et al. 2014). In a group of radio galaxies, the shallow optical depth ($\tau < 0.05$) and the blue-shifted wings of the H I absorption lines trace a fast outflow of neutral hydrogen driven by the expansion of the radio jets (e.g. Morganti et al. 2005a, 2013a; Kanekar & Chengalur 2008; Mahony et al. 2013; Geréb et al. 2015; Allison et al. 2015).

Absorption studies also have the advantage of allowing us to detect the gas using relatively short radio observations and reaching higher redshifts than emission studies, since the detection in absorption does not depend on the redshift of the source but only on the strength of the radio background continuum. Thus, H I absorption studies allow us to study the impact of the radio nuclear activity on the ISM in a variety of radio sources (e.g. Vermeulen et al. 2003; Pihlström et al. 2003; Gupta et al. 2006; Emonts et al. 2010; Allison et al. 2012, 2014; Chandola et al. 2013; Geréb et al. 2014, 2015; Chandola & Saikia 2017; Glowacki et al. 2017; Curran et al. 2017). Among several results, these studies show that in compact steep spectrum sources (CSS) and gigahertz peaked sources (GPS), (i.e. sources that possibly represent young radio AGN; Fanti et al. 1995; Readhead et al. 1996; O'Dea 1998) the H I is detected more often. Collecting a large sample also allows us to perform stacking experiments on the sources where the H I is not detected, thus providing a complete characterisation of the content of H I in radio AGN. Through this technique, Geréb et al. (2014) show that in the direct non-detections, the H I if present, it must have very low optical depths ($\tau \lesssim 0.002$) compared to the detections, suggesting a dichotomy in the properties of the neutral hydrogen in radio-loud early-type galaxies.

Until now, to obtain a good trade-off between sensitivity and observing time, H I absorption surveys have been focussing on the high-power radio sources ($\log P_{1.4\,\mathrm{GHz}} > 24\ \mathrm{W\,Hz^{-1}}$), but low-power sources ($\log P_{1.4\,\mathrm{GHz}} < 24\ \mathrm{W\,Hz^{-1}}$) in early-type galaxies form the bulk of the radio AGN population (Bahcall et al. 1997; Best et al. 2005; Sadler et al. 2007). Hence, to fully understand the importance of radio AGN in galaxy evolution scenarios it is crucial to investigate the interplay between the radio activity and ISM among sources of all radio powers.

Here, we expand the work of Geréb et al. 2014, 2015 (hereinafter G14 and G15) by extending the sample to low radio powers, i.e. $\log P_{1.4\,\mathrm{GHz}} = 22.5\ \mathrm{W\ Hz^{-1}}$. The final sample combines the sample of G14 and G15 with the sample presented here and includes 248 sources. The survey presented here was constructed to observe all the objects in a uniform way and to reach, even for the weakest sources of the sample ($S_{1.4\,\mathrm{GHz}} \sim 30$ mJy), optical depths of a few percent. The survey also provides a statistically significant sample in preparation of future H I absorption surveys, which are about to start with the SKA pathfinders and precursors.

We carried out the observations of our sample with the Westerbork Synthesis Radio Telescope (WSRT) between December 2013 and February 2015. Over the same period, the dishes of the telescope were refurbished and the receivers upgraded to the phased array feed system, Apertif (Oosterloo et al. 2010b). Since the observations of this survey were carried out up to the very last hours before the telescope closed for the final upgrade, this survey is the last one undertaken with the old WSRT.

This paper is structured as follows. In Sect. 2.1 we outline the selection of the sample and describe the 1.4 GHz observations, while in Sect. 2.2 we discuss how we can classify our sources depending on their mid-infrared (MIR) colours and the extension of their radio continuum emission. In Sect. 3 we report the results of the survey. In particular, we analyse the occurrence of H I in the sample (Sect. 3.1), we determine the main properties of the detected absorption lines (Sect. 3.2), and we perform stacking experiments to search for low column density H I, which is undetectable by single observations (Sect. 3.3). Section 4 discusses the results of this survey focussing on the impact of the radio source on the H I of the host galaxies. In Sect. 5 we use the results from this work to predict how many and what type of HI absorbers the upcoming surveys with the Square Kilometre Array pathfinders may produce. Section 6 summarises our results and conclusions. In Appendix A, we show the new H I absorption lines we detected in the survey (see Fig. A.1) and the main properties of all sources of the sample, such as redshift, radio continuum flux, and radio power (see Table A.1).

Throughout this paper we use a ΛCDM cosmology, with Hubble constant $H_0 = 70\ \mathrm{km\ s^{-1}\,Mpc^{-1}}$ and $\Omega_\Lambda = 0.7$ and $\Omega_\mathrm{M} = 0.3$.

2. Description of the sample

2.1. Sample selection and observations

We expand the sample of radio sources presented in G14 and G15 to lower radio fluxes and radio powers. As in those studies, we selected the sources by cross-correlating the seventh data release of the Sloan Digital Sky Survey catalogue (SDSS DR7; York et al. 2000) with the Faint Images of the Radio Sky at Twenty-cm catalogue (FIRST; Becker et al. 1995). The sources lie above declination $\delta > 10°$ and between $07^\mathrm{h}51^\mathrm{m}00^\mathrm{s}$ and $17^\mathrm{h}22^\mathrm{m}25^\mathrm{s}$ in right ascension. The sources are restricted to the redshift range $0.02 < z < 0.25$, which is the redshift interval covered by the WSRT observing band, 1150–1400 MHz. The sample of G14 and G15 was limited to sources brighter than 50 mJy and consists of 101 sources. In the present study, we selected all sources that have radio core flux density 30 mJy $< S_{1.4\,\mathrm{GHz}} <$ 50 mJy. This includes 219 sources, of which 183 were successfully observed before the telescope was switched off for the upgrade of the receivers.

In 37 objects the observed band was affected by strong radio interference making the data unusable. One source of 353 mJy (J082133.60+470237.3) was not included in SDSS DR7, but its spectrum became available with the DR9 data release. This source falls in the field of view of the observation of J082209.54+470552.9, and we include it in the final sample of 147 sources.

The observations were carried out in the period December 2013–Feb. 2015 (proj. num. R14A019 and R14B006). We used a similar set-up of the telescope as in G14 and G15. We also did not use a full synthesis (12 h) in order to observe as many objects as possible. However, given that fewer WSRT dishes were available at the time of our observations and to maintain the same sensitivity as in G14 and G15, in all observations we increased the integration time to six hours per source. The observational set-up consists of 1024 channels covering a bandwidth of 20 MHz.

We reduced the data following a similar procedure to that presented in G14 and G15 via the `MIRIAD` package (Sault et al. 1995). The final H I data cubes have a velocity resolution of 16 km s^{-1}. The median noise of the final spectra is 0.81 mJy beam^{-1} and ~90% of the observations have a noise level lower than 1.3 mJy beam^{-1}. We created continuum images using the line-free channels to measure the continuum flux density of the sources. However, because of the limited uv coverage

of the observations, the beam of the observations is very elongated, typically about 45″ × 12″. In Table A.1 we report a full summary of the main radio properties of the sources.

For the analysis that follows, we combine the newly observed 147 low-power sources (30 mJy < $S_{1.4\,\mathrm{GHz}}$ < 50 mJy) with the 101 sources with $S_{1.4\,\mathrm{GHz}} > 50$ mJy presented in G14 and G15, obtaining a sample of 248 sources.

2.2. Characterisation of the AGN sample

One goal of this survey is to determine the occurrence and properties of H I for the different types of radio sources present in our sample. The sources of our sample lie in the massive end of the red sequence ($-24 < M_r < -21$, $u-r \sim 2.7 \pm 0.6$). Nine sources are an exception ($u-r \lesssim 2$). Their SDSS images show that they are undergoing a merger with a spiral galaxy or that they have large tails of gas and stars, suggesting a recent or ongoing interaction with a companion. These sources are different from the bulk of our sample of early-type radio galaxies, hence, from here on, we classify them as interacting and we denote them with grey diamonds in all figures.

The MIR colours allow us to classify the galaxies according to their dust content. For such a purpose, different studies (e.g. Wright et al. 2010; Stern et al. 2012; Jarrett et al. 2013; Mingo et al. 2016) have used data from the all-sky Wide-field Infrared Survey Explorer (WISE), which observed in four MIR bands, i.e. 3.4 μm (W1), 4.6 μm (W2), 12 μm (W3), and 22 μm (W4). The W3 band is sensitive to the dust continuum and the presence of polycyclic-aromatic hydrocarbons (PAHs), whose emission lines peak at 11.3 μm and may trace the star formation activity in a galaxy (Lee et al. 2013; Cluver et al. 2014). The luminosity at 12 μm of dust-poor red-sequence galaxies is dominated by the old stellar population and is similar to the luminosity at 4.6 μm, whereas galaxies rich in PAHs and dust have enhanced luminosity at 12 μm, which increases their W2–W3 colour. Starburst galaxies typically have W2–W3 > 3.4 (e.g. Rosario et al. 2013). The W1–W2 colour is sensitive to heated dust. When an AGN is present, as in the sources of our sample, galaxies bright at 4.6 μm are likely to have a dust-rich circumnuclear region that is heated by the nuclear activity.

In this study, we cross-matched the sky coordinates of each source with the WISE catalogue to extract the WISE magnitudes, making use of the VizieR catalogue access tool (Ochsenbein et al. 2000). We followed Mingo et al. (2016) to distinguish between so-called dust-poor sources (W1–W2 < 0.5 and W2–W3 < 1.6) and galaxies with MIR emission enhanced by the dust continuum and PAHs, which we call 12 μm bright sources (W1–W2 < 0.5 and 1.6 < W2–W3 < 3.4); AGNs with hot dust in the circumnuclear regions (W1–W2 > 0.5); and dust-rich starburst galaxies (W1–W2 < 0.5 and W2–W3 > 3.4). Given that there are only three starburst galaxies in our sample, with W1–W2 ∼ 0.5, we include them in the sample of AGN rich of heated dust, which we name 4.6 μm bright sources because of their enhanced flux at this wavelength. In the following sections, we sometimes use the generic name MIR bright sources to refer to 12 μm bright and to 4.6 μm bright sources altogether.

As shown in Fig. 1 and Table 1, half of the sources are classified as dust-poor (52%, indicated by green squares in this and the following figures) while 27% are 12 μm bright sources (indicated by orange pentagons). Forty-two sources (17%) are classified as 4.6 μm bright galaxies (indicated by black triangles).

Following G14, we classified the radio continuum emission of the sample depending on the NVSS major-to-minor axis ratio

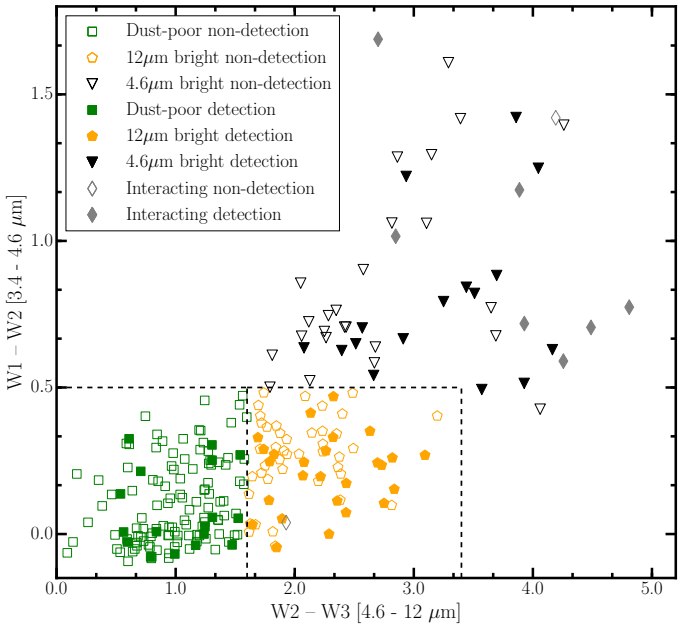

Fig. 1. WISE colour–colour plot for the sources of the sample, separated into H I detections (filled symbols) and H I non-detections (empty symbols). Dust-poor galaxies are green squares, 12 μm bright sources are orange pentagons and 4.6 μm bright sources are black triangles. Interacting sources are grey diamonds. The dashed lines indicate the cut-offs of the WISE colours we used to classify our sources. Further details on the classification of the sources are shown in Table 1.

versus the FIRST peak-to-integrated flux ratio. Figure 2 and Table 1 show the classification for the sample of 248 sources, where we designate 52% as compact sources (in red in the figure) and 48% as extended sources (in blue). Compact sources typically have the radio continuum embedded in the host galaxy at sub-galactic scales (≲few kilo-parsec), while extended sources have radio continuum at super-galactic scales. For a group of radio AGN, the extent of their radio continuum emission can be related to the age of the nuclear activity. Compact steep spectrum sources (CSS) and gigahertz peaked sources (GPS) are the youngest family of radio AGN (O'Dea 1998; Murgia 2003; Fanti 2009; Sadler 2016; Orienti 2016), and in general, they can be considered younger radio AGN than extended sources. A fraction of the compact sources of our sample belong to this group of young radio AGN (see G14 and G15).

3. Results

From the new observations presented in this paper (objects with radio flux between 30 mJy < $S_{1.4\,\mathrm{GHz}}$ < 50 mJy), we detect H I absorption in 34 galaxies with 3σ significance above the noise level. Since the observations are relatively shallow, for the weaker radio sources ($S_{1.4\,\mathrm{GHz}} \sim 30$ mJy) we are sensitive to absorption lines with peak optical depth of $\tau_{\mathrm{peak}} \sim 0.08$.

Following G15, we use the busy function (BF; Westmeier et al. 2014) to measure the main properties of the lines in a uniform way, i.e. centroid, peak optical depth (τ_{peak}), integrated optical depth ($\int \tau dv$), full width at half-maximum (FWHM), and full width at 20% of the peak flux (FW20). The detected lines and fits produced by the BF are shown in Fig. A.1. In Table A.1 we summarise these parameters for each detection.

In the following, we discuss the results making use of the full sample by combining the new data and the G14 and G15 data.

Table 1. Statistics of the sample.

	Number of sources	Non-detections	Detections	Detection rate (%)
All sources	248	182	66	27 ± 5.5
Radio continuum classification				
Compact sources	131	89	42	32 ± 7.9
Extended sources	108	91	17	16 ± 6.8
WISE colour classification				
Dust-poor sources	129	112	17	13 ± 5.8
12 μm bright sources	68	42	26	38 ± 11
4.6 μm bright sources	42	26	16	38 ± 16
Interacting sources	9	2	7	78 ± 27

Notes. Number of observed sources (1), number of H I absorption non-detections (2), number of H I detections (3), and detection rates (4) for all sources and different subsamples of compact and extended sources, based on the radio-continuum classification (see Fig. 2), dust-poor, 12 μm bright and 4.6 μm bright sources, according to the WISE colour–colour plot (Fig. 1), and interacting sources.

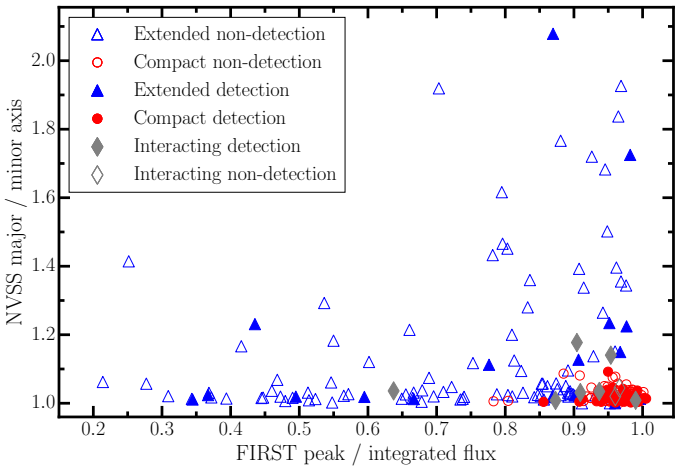

Fig. 2. Radio morphological classification of the sample. Red circles indicate compact sources, extended sources are indicated by blue triangles, interacting sources are shown in grey diamonds. H I detections are indicated by filled symbols, while empty symbols represent non-detections.

3.1. Occurrence of H I in radio sources

Considering the full sample, we detected H I absorption in 66 sources out of 248, leading to a detection rate of 27% ± 5.5%[1]. Compared to G14 and G15, we have now extended the range of the sample to low radio powers (down to log $P_{1.4\,\mathrm{GHz}}$= 22.5 W Hz^{-1}), and it is worth mentioning that, albeit with small number statistics in some of the bins, the detection rate is similar across the range of radio powers covered by the survey, as illustrated in the top left panel of Fig. 3. The top right panel of the figure shows that we detect H I absorption lines, with a peak that is three times above the noise level, in sources throughout the entire range of fluxes. The bottom left panel shows that we detect H I in all redshift intervals. The absorption lines have a broad range in peak optical depths, i.e. approximately between 0.3 and 0.003 (bottom right panel), and we detect lines across the full range of optical depths to which we are sensitive. These results confirm and extend what already observed in the subsample of higher flux sources ($S_{1.4\,\mathrm{GHz}} > 50$ mJy) of G14 and G15.

In Table 1, we show the detection rate of H I absorption depending on the classification of their radio continuum emission and of their WISE colours. We detect H I in all different types of galaxies but with different detection rates. In the sources that we classify as compact, H I is detected twice as often as in the extended sources (32% ± 7.9% and 16% ± 6.8%, respectively). This behaviour was also observed in G14 and in previous works on smaller and less homogeneously selected samples (e.g. Emonts et al. 2010; Curran et al. 2011, 2013a,b).

For dust-poor galaxies the detection rate is low (13% ± 5.8%) compared to 12 μm bright sources (38% ± 11%) and 4.6 μm bright galaxies (38% ± 16%).

3.2. Kinematics of H I

Figure 4 shows the FW20 of the H I absorption lines versus the radio power of the sources. The dashed horizontal line indicates the mean of the distribution of rotational velocities of the sample[2]. The fine dashed horizontal line indicates the 3σ value of the distribution of the rotational velocities. In this study, we consider an H I line broad when it has FW20 above this latter line. When a line is broad, the H I cannot simply rotate within the galaxy, but it must also have a component with non-ordered kinematics. At high radio powers (log $P_{1.4\,\mathrm{GHz}} > 24$ W Hz^{-1}), 30% ± 15% of the lines are broad.

Figure 5 shows the shift of the centroid of the line with respect to the systemic velocity of the galaxy versus the radio power of the sources. At low radio powers (log $P_{1.4\,\mathrm{GHz}} <$ 24 W Hz^{-1}), the majority of the lines are centred at the systemic velocity (Δv ± 100 km s^{-1}). At log $P_{1.4\,\mathrm{GHz}} > 24$ W Hz^{-1}, 36% ± 16% of the lines are offset with respect to the systemic velocity.

As shown in the left panel of Fig. 4, broad lines are found only in compact radio sources. One exception is 3C 305, which is classified as extended according to our classification, but is known to be a compact steep spectrum source of 4 kpc in size (Jackson et al. 2003). The broad H I is known to trace a fast outflow (Morganti et al. 2005a), which is consistent with what found in this paper.

[1] We compute the errors on the detection rates as the 95% confidence level of a binomial proportion.

[2] We determine the rotational velocity of the sources from their K magnitude using the Tully-Fisher relation for red-sequence galaxies (den Heijer et al. 2015) and correcting for the average inclination of the sources, measured from the axis ratio of the stellar body of the host galaxies.

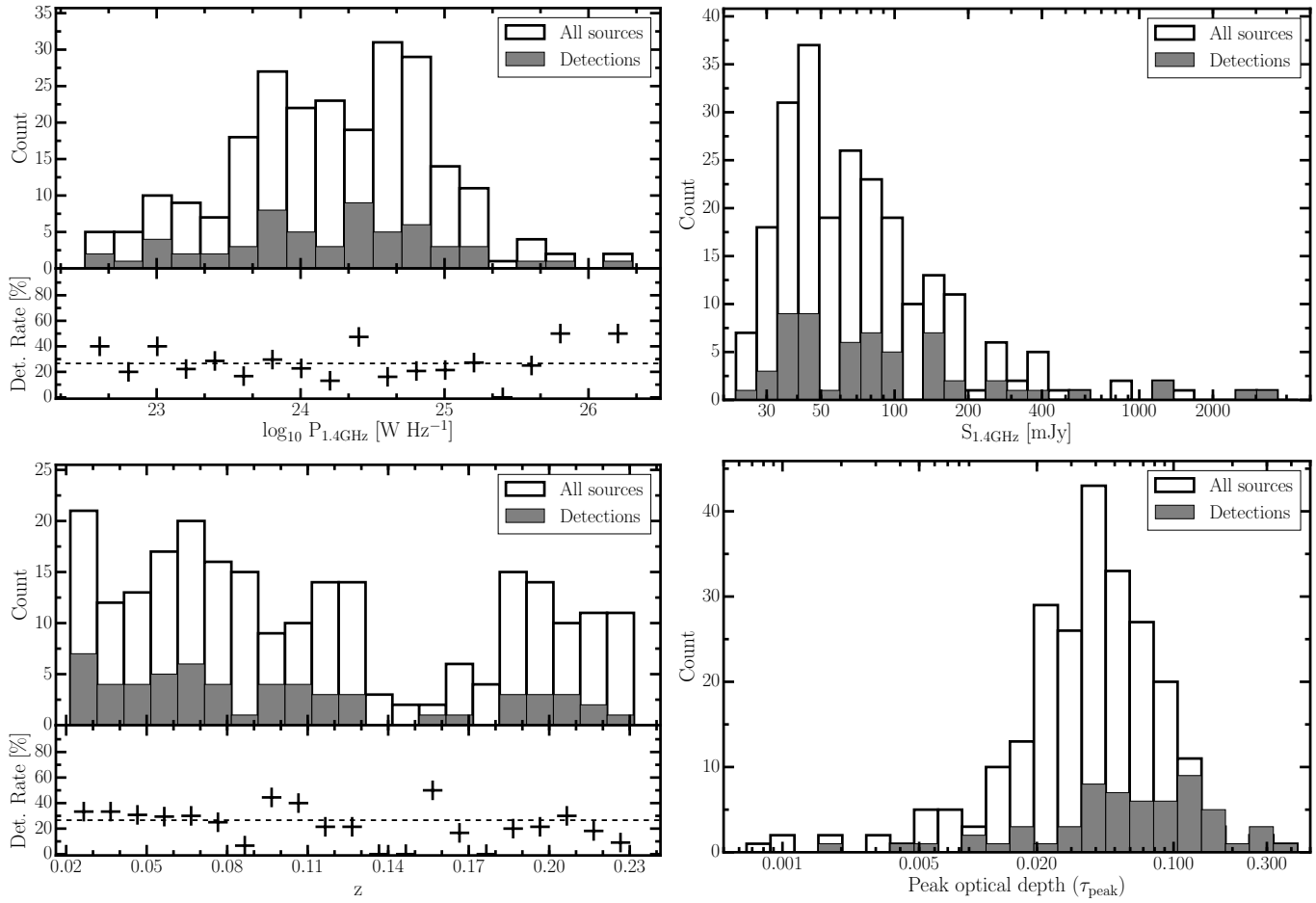

Fig. 3. *Top left panel*: radio power distribution of the full sample and the detections. The sub-panel below shows the detection rate for each bin of the histogram and the average detection rate (dashed line). *Top right panel*: radio continuum flux ($S_{1.4\,\mathrm{GHz}}$) distribution of the full sample (open bars) and of the detections (grey bars). *Bottom left panel*: redshift (z) distribution of the full sample of 248 radio sources and of the H I detections. The sub-panel shows the detection rate for each bin of the histogram. *Bottom right panel*: distribution of the optical depth detection limits of the full sample overlaid with the distribution of the optical depth of the peak of the detected absorption lines.

The lines that are broad in Fig. 4 also have a shifted centroid. This because, as shown in G15, these lines have, apart from a main component, a second, shallower component that extends to blue-shifted velocities, which we call wing. Interestingly, the majority of these wings are blue-shifted indicating that there is at least a component of the gas outflowing.

At low radio powers (log $P_{1.4\,\mathrm{GHz}} < 24$ W Hz^{-1}), we only detect relatively narrow lines with the exception of the interacting galaxies. At the sensitivity of our observations, we would have not been able to detect broad and shallow wings with ratio between the wing and peak of the absorption line <0.3, as they would have been hidden in the noise. We know that in some low-power radio sources, for example NGC 1266 (Alatalo et al. 2011) and IC 5063 (Oosterloo et al. 2000; Morganti et al. 2013b, 2015), H I outflows can be present and are traced by a broad and shallow ($\tau < 0.005$) blue-shifted wing in the absorption line. If these shallow and broad wings were present in the HI lines of the low-power sources, we would not have detected them. Despite this limitation, it is interesting to see that the great majority of the lines in low power sources are centred on the systemic velocity (Fig. 5). This means that the dominant component traced by the H I absorption is associated with settled gas.

In Fig. 4 (right panel), we show FW20 versus the radio power of the sources, classifying sources according to their WISE colours (see Fig. 1). Dust-poor sources do not show broad lines. Mid-infrared bright sources (both at 12 μm bright and at 4.6 μm) have broad lines if the radio power is log $P_{1.4\,\mathrm{GHz}} > 24$ W Hz^{-1}.

Figure 6 shows the FW20 versus the integrated optical depth of the line, classifying the sources according to their WISE colours. In dust-poor sources, we only detect narrow H I lines (FW20 < 300 km s^{-1}) with integrated optical depth $\gtrsim$1.5 km s^{-1}. In 12 μm bright and 4.6 μm bright galaxies we detect both shallow and broad lines. The histogram at the top of the figure shows the estimated upper limit to the integrated optical depth of the non-detections of each subgroup of galaxies. For each source, this is equal to three times the noise of the spectrum in optical depth times the mean width of the detected lines (145 km s^{-1}). For most dust-poor galaxies the detection limit is $\int \tau dv > 1.5$ km s^{-1}. For ten dust-poor sources the detection limit is lower and should allow us to detect the shallow broad lines that we detected in the other sources, but we detect none in these ten sources. This suggests that in dust-poor sources the H I traced by the broad and shallow wings of the lines is absent.

3.3. Stacking in search for H I absorption

Sources where we do not directly detect an absorption line may still have H I that can be uncovered with stacking techniques. In a stacking experiment, the noise of the final stacked spectrum

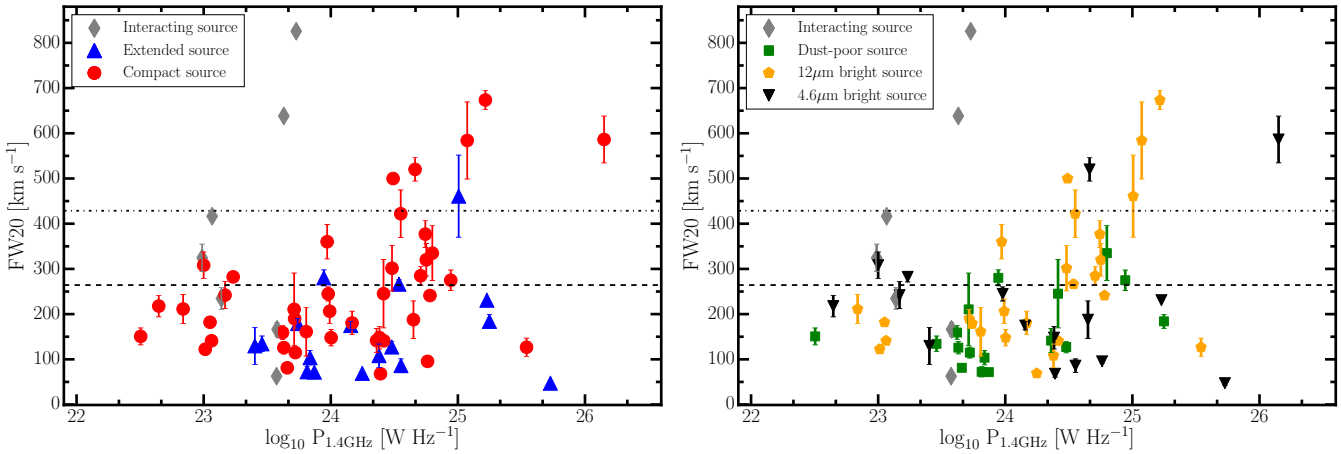

Fig. 4. *Left panel*: full width at 20% of the intensity (FW20) of the H I profiles vs. the radio power of the sources. Sources are classified according to the extension of their radio continuum (see Fig. 2). The dashed line indicates the mean of the distribution of rotational velocities of the sources of the sample. The fine dashed line shows the 3σ upper limit of the distribution (see Sect. 3.2 for further details). *Right panel*: same as in the *left panel* with symbols following the WISE colour–colour plot shown in Fig. 1.

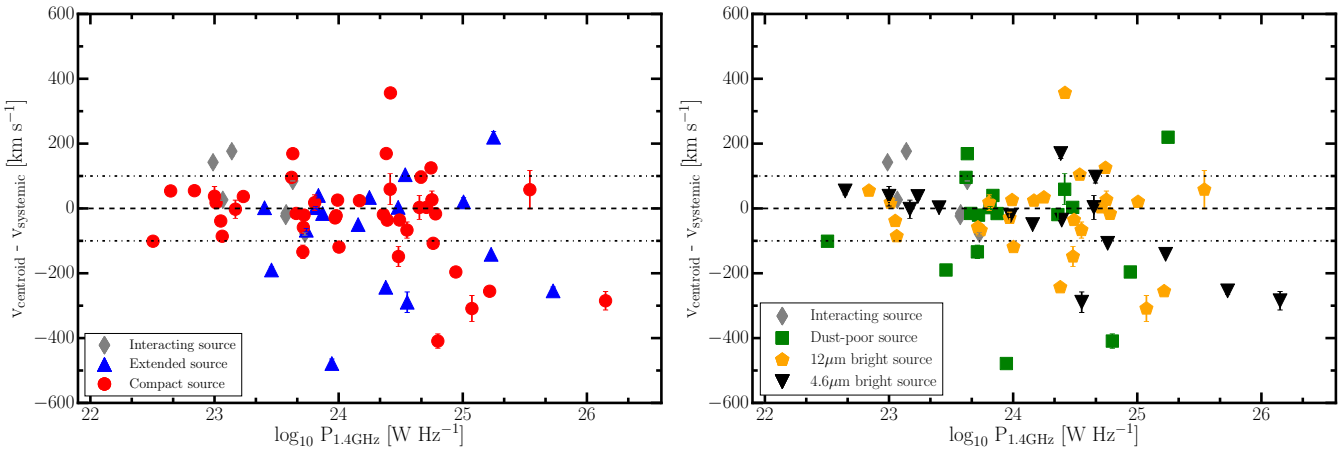

Fig. 5. *Left panel*: blue shift and red shift of the H I line centroid with respect to the systemic velocity vs. the radio power of the sources. Sources are classified according to the extent of their radio continuum (see Fig. 2). The fine dashed lines indicate the ± 100 km s^{-1} velocities. *Right panel*: same as in the left panel with symbols following the WISE colour–colour plot shown in Fig. 1.

decreases with the square root of the number of stacked spectra. Stacking the non-detections of our sample allows us to explore the statistical presence of H I absorption at low optical depths.

In G14, we stacked the spectra of 66 non-detections with $S_{1.4\,\mathrm{GHz}} > 50$ mJy, reaching a detection limit of $\tau \sim 0.002$ (3σ) without detecting any absorption. In this study, we stack 170 non-detections of the sample. We stack the spectra in optical depth aligning them at the SDSS redshift. Figure 7 (left panel) shows the final co-added spectrum. We reach a detection limit of $\tau = 0.0015$ (3σ), without detecting any line. A non-detection at such low optical depth confirms the results of G14. There, we pointed out that the peak optical depth of the detected H I lines is much higher than the detection limit reached by the stacking experiment. This suggests a dichotomy between H I detections and H I non-detections. In the latter, if H I is present, it must have much lower column densities or higher spin temperature (T_{spin}) than in the former.

In Sect. 3.1, we point out that the detection rate of H I in absorption is higher in compact sources than in extended sources. Likewise, it is higher in MIR bright sources than in dust-poor sources. Here, we explore whether this can also be seen by stacking the undetected objects belonging to these groups.

We do not detect any absorption line either by stacking the spectra of the compact non-detections (72 sources) or extended non-detections (80 sources); see Fig. 7 (middle panel). We do not detect any line either by stacking the dust-poor non-detections (97 sources) or the MIR bright non-detections (71 sources), see Fig. 7 (right panel). In Table 2, we show the 3σ detection limits of the stacked spectra for these subgroups. On average we reach a detection limit of $\tau \sim 0.003$. These results suggest that a dichotomy in the presence of H I holds among all kinds of radio sources in agreement with the dichotomy observed in the stacking experiment of all non-detections.

4. Discussion

4.1. H I morphologies and kinematics in different radio AGN

H I absorption has been studied in radio AGN for many years. Previous works (e.g. van Gorkom et al. 1989; Morganti et al. 2001, 2005b; Vermeulen et al. 2003; Gupta et al. 2006) have already suggested the possibility of a range of structures of the absorbing material that can, to the first order, be identified from the shape of the absorption lines. In some cases, this has been

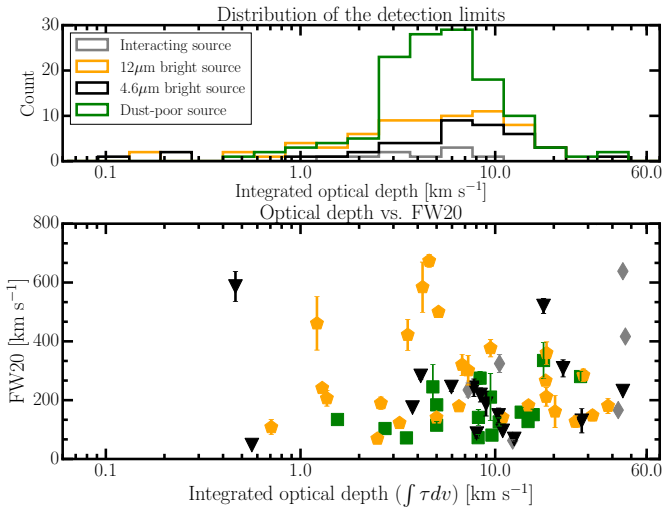

Fig. 6. Full-width at 20% of the intensity (FW20) vs. the integrated optical depth of the H I lines ($\int \tau dv$). Symbols follow the WISE colour–colour classification shown in Fig. 1. The histogram in the *top panel* shows the distribution of the 3σ detection limit in optical depth for the non-detections of the each subsample.

verified with follow-up high-resolution observations or by H I emission observations (Beswick et al. 2004; Struve & Conway 2010; Struve et al. 2010; Mahony et al. 2013; Maccagni et al. 2014).

Absorption lines detected against the nuclear radio component and close to the systemic velocity with narrow (<100 km s^{-1}) widths are likely the result of large-scale gas disks (e.g. dust lanes) while broader profiles (a few hundred km s^{-1}) can result from a circumnuclear disk, such as Cygnus A (Conway & Blanco 1995; Struve & Conway 2010) and Centaurus A (van der Hulst et al. 1983; Struve et al. 2010; Struve & Conway 2012). Distinguishing these structures is not straightforward because, as for all absorption studies, the shape and width of the line also depend on the structure of the background radio continuum.

Absorption lines with centroid offset with respect to the systemic velocity or lines with a broad (e.g. beyond the expected rotational velocity) red-shifted or blue-shifted wing, can trace gas that is unsettled, either infalling or outflowing, as in, for example NGC 315 (Morganti et al. 2009) PKS B1718–649 (Maccagni et al. 2014), B2 1504 +377 (Kanekar & Chengalur 2008), NGC 1266 (Alatalo et al. 2011), 4C 12.50 (Morganti et al. 2013b), and PKS B1740-517 (Allison et al. 2015).

In this work, we relate the H I morphologies traced by the 66 detected absorption lines of our sample to the radio power, extent of the radio continuum, and MIR colours of the associated host galaxies. Figure 4 shows that in sources with log $P_{1.4\,\mathrm{GHz}}$ < 24 W Hz^{-1}, we only detect narrow lines (excluding interacting sources, see Sect. 2.2), while at log $P_{1.4\,\mathrm{GHz}}$ > 24 W Hz^{-1} we also detect lines that are broad because of an asymmetric wing (with wing-to-peak ratio $\gtrsim$0.3). Figure 5 shows that at radio powers below 10^{24} W Hz^{-1} the lines are centred at the systemic velocity, while above this threshold, the broad lines are also offset by more than ±100 km s^{-1}. This suggests that, in our sample, in sources with log $P_{1.4\,\mathrm{GHz}}$ < 24 W Hz^{-1} the H I lines trace a large-scale rotating disk, while in more powerful sources the H I is not only rotating but it can also have unsettled kinematics. If in a low power source, a broad line had wing-to-peak ratio <0.3, the broad wing would have not been detected at the sensitivity of our observations. Cases of lines with such broad, shallow, and blue-shifted wings are known to be present in low-power sources, such as NGC 1266 (Alatalo et al. 2011) and IC 5063 (Oosterloo et al. 2000; Morganti et al. 2013b, 2015). However, since these wings are very shallow, they do not affect the FW20 of the bulk of the line, where the peak lies. Hence, we can confirm that the deep absorption is on average narrower in low-power sources.

Figures 4 and 5 also show that the sources where the H I is unsettled have compact radio continuum (left panels), and are MIR bright (right panels). Figure 6 shows that in dust-poor galaxies we do not detect unsettled gas but only narrow and deep H I absorption lines. These results suggest that in dust-poor sources the H I may be rotating in a disk. If, instead, the radio AGN is powerful (log $P_{1.4\,\mathrm{GHz}}$ > 24 W Hz^{-1}) and compact, i.e. the jets are embedded within the host galaxy and the host galaxy is MIR bright, then the H I may have unsettled kinematics, which possibly originates from the interplay between the radio activity and surrounding cold gas.

4.2. Stacking experiment and comparison with the ATLAS^{3D} sample

The absorption lines detected in our sample show that, depending on the radio power, they may trace H I with different kinematics. Nevertheless, the H I is detected with a detection rate of 27% ± 5.5% that is independent of the radio power of the sources (see Sect. 3.2). The results of the stacking experiment have shown no detection of H I absorption, even after expanding the number of stacked sources compared to G15 (see Sect. 3.3). This confirms a dichotomy in the presence and/or properties of H I in radio AGN. For the detections, the peak of the absorption is often found at high optical depths ($\tau \gtrsim 0.01$). In the non-detections, if H I is present, then this peak must have a much lower optical depth than in the detections or its detection must be affected by orientation effects.

In order to investigate the origin of this dichotomy, we compare our results with what is found for H I emission, i.e. not affected by orientation effects and not limited by the size of the continuum emission. We use the ATLAS^{3D} sample (Cappellari et al. 2011) because it represents the only complete volume-limited sample of early-type galaxies of the local Universe (i.e. objects similar to the host galaxies of our radio sources) with deep H I observations (Oosterloo et al. 2010a; Serra et al. 2012). The ATLAS^{3D} sources represent the low radio-power end of our sample, since they have log $P_{1.4\,\mathrm{GHz}}$ < 22.5 W Hz^{-1} (Nyland et al. 2017) and lie at fainter magnitudes in the red sequence than our sample ($-21.5 < M_r < -19$) . Among the ATLAS^{3D} sources, 139 were observed in H I. H I has been detected in emission in the centre of 25% of these sources, i.e. in the same region where we search for H I in the sources of our sample. In most cases, the H I appears settled in disk and ring morphologies, but there are many exceptions. H I is not detected in the centre of 81 galaxies. A stacking experiment on these sources allows us to determine the typical H I column density, or its upper limit, in the centre of early-type galaxies.

Before stacking, we convert each spectrum to column density, correcting for the beam (θ, in arcminutes) of the observation,

$$N_{\mathrm{H\,I}} \sim 3.1 \times 10^{17} \cdot S \cdot \mathrm{d}v/\theta^2,$$

where S is the flux per channel (dv). In Fig. 8, we show the result of stacking the H I spectra of the 81 non-detections. An emission

Table 2. Statistics of the stacking experiment.

Sample	Number of sources	3 × rms [optical depth]
Non-detections	170	0.0015
Compact	72	0.0033
Extended non-detections	80	0.0027
4.6 μm bright and 12 μm bright non-detections	71	0.0033
Dust-poor non-detections	97	0.0027

Notes. Results of the stacking experiment for the non-detections and their subsamples based on the radio classification (compact and extended sources) and on the WISE colour–colour plot (4.6 μm bright, 12 μm bright and dust-poor galaxies). Since no lines are detected in absorption, we provide as upper limits three times the noise level of the final stacked spectrum.

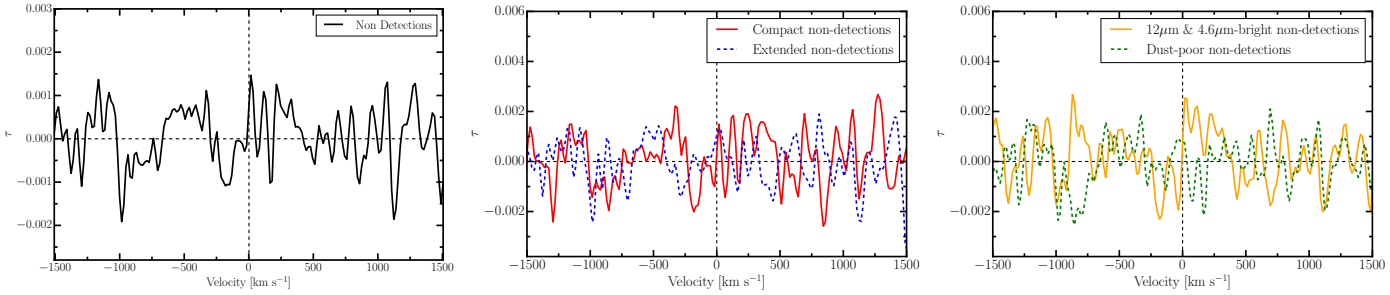

Fig. 7. *Left panel*: stacked spectrum of 170 non-detections. *Middle panel*: stacked spectrum of 72 non-detections with compact radio emission or interacting sources (red) and of 80 non-detections with extended radio emission (blue). *Right panel*: stacked spectrum of 71 non-detections classified as 12 μm bright or 4.6 μm bright galaxies (orange), and of 97 non-detections classified as dust-poor (green), according to the WISE colours.

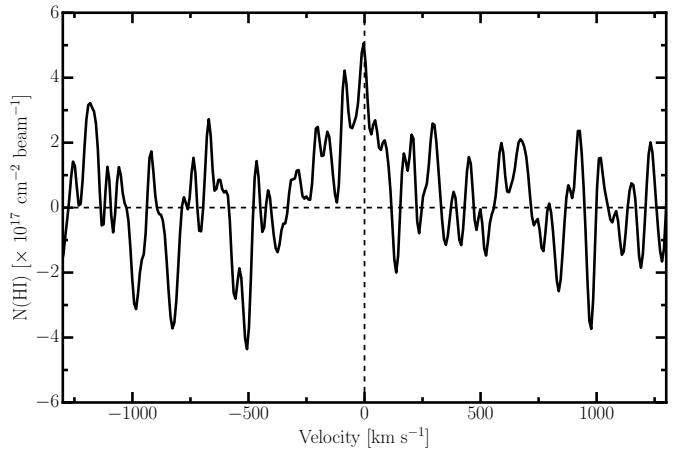

Fig. 8. Stacking in column density of the spectra of 81 ATLAS^{3D} sources undetected in H I emission.

line is detected with ~3σ significance at the systemic velocity. The FWHM of the line is ~200 ± 50 km s^{-1}.

The detection of H I in the early-type galaxies of ATLAS^{3D} shows that the majority have a low amount of H I that is below the typical detection level but that can be recovered by stacking. We use this detection to derive the corresponding optical depth if this gas would have been observed in absorption. The integrated column density of the emission line is $N_{\rm H\,I} \sim 2.1 \times 10^{19}$ cm^{-2}. The corresponding optical depth can be estimated as

$$\tau \sim \frac{N_{\rm H\,I}}{1.8216 \times 10^{18} \times FWHM \times T_{\rm spin}/c_f} \sim 0.06 \times \frac{c_f}{T_{\rm spin}},$$

where c_f is the covering factor, i.e. the fraction of radio continuum covered by the absorbed gas, and $T_{\rm spin}$ is its spin temperature. The spin temperature of the H I can range between a few 10^2 K in the extended disks to a few 10^3 K in the central regions of AGN (Maloney et al. 1996; Kanekar et al. 2003, 2011; Holt et al. 2008; Morganti et al. 2016). The detection limit we reach by stacking the spectra of our sample ($\tau = 0.0015$, see Table 2) can be converted to a column density, assuming that the width of the absorption line is equal to the width of the emission line of the stacked ATLAS^{3D} sources. This column density is $N_{\rm H\,I} = 3.5 \times 10^{17}\,(T_{\rm spin}/c_f)$ cm^{-2}. For $T_{\rm spin} \gtrsim 100$ K and $c_f = 1$, this value is higher than the column density of the emission line of the stacked ATLAS^{3D} sources. Therefore, the stacking experiment in absorption cannot detect the low-column density gas we detect in the ATLAS^{3D} sources. If a similar amount of H I as in the stacked ATLAS^{3D} galaxies was present in our radio galaxies, we would expect (assuming $c_f = 1$) H I absorption in the stacked profile with optical depth in the range $\tau \sim 10^{-4}$ for $T_{\rm spin} \sim 100$ K and $\tau \sim 10^{-5}$ for higher temperatures, for example $T_{\rm spin} \sim 10^3$ K. These values are approximately three times lower than the detection limit we found in the stacking experiment for our sample (see Table 2). Thus, the stacking of our radio galaxies does not reach yet the sensitivity necessary to detect an amount of H I that is comparable to what was detected for the ATLAS^{3D}. Achieving these limits will only be possible with the larger samples provided by the new surveys (see Sect. 5).

From the amplitude of the H I detection obtained by stacking the ATLAS^{3D} sources, we can infer that the dichotomy between early-type galaxies with detected and undetected H I could be due to a difference in the amount of H I between the two groups. The H I detected in emission in the ATLAS^{3D} galaxies (and column-density limited) is likely tracing only H I in large galactic-scale structures. As described above, H I absorption can also trace gas that is distributed in small scale, nuclear structures as its detection depends only on the strength of the background continuum. Thus, in the case of absorption, other effects can affect the non-detection of H I. These effects can be orientation effects, H I depletion in the nuclear region, or when only the

warm component of H I (i.e. low optical depth for a given column density) is intercepted along the line of sight.

In compact sources the radio emission is embedded within the host galaxy hence the detection of absorption should be less affected by orientation effects of the absorbing structure (Pihlström et al. 2003; Curran et al. 2013a). However, the stacking experiment of this class of objects does not reveal an absorption line down to $\tau \sim 0.003$. This may suggest that orientation effects are not the only explanation of why H I is detected (or not) in absorption. Nevertheless, among two subsamples of sources we find hints that orientation effects contribute in detecting H I absorption. In Fig. 10 of G14 we show that among the high-power sources ($\log P_{1.4\,\mathrm{GHz}} > 24\,\mathrm{W\,Hz^{-1}}$) in the most highly inclined galaxies (axial ratio of the stellar disk, measured by SDSS, $b/a < 0.6$), we always detect H I at high column densities ($N_{\mathrm{H\,I}} \gtrsim 10^{19} \cdot c_f/T_{\mathrm{spin}}\ \mathrm{cm^{-2}}$). Among more face-on galaxies ($b/a < 0.6$), we do not always detect H I; when we detect H I the absorption lines can have lower column densities than in edge-on sources. When a source is 4.6 μm bright, the WISE colours (W2–W4) allow us to estimate the orientation of the circumnuclear dust with respect to the AGN (Crenshaw et al. 2000; Fischer et al. 2014; Rose et al. 2015). Among the 42 4.6 μm bright sources of our sample, 28 have W2–W4 < 6, which suggests an unobscured AGN, i.e. the circumnuclear dust is face-on with respect to the line of sight, while 14 have W2–W4 > 6, which suggests an obscured AGN, i.e. the circumnuclear dust is edge-on with respect to the line of sight. Among obscured AGN the detection rate of H I is 50% ± 25%, while in unobscured AGN the detection rate is 32% ± 17%. These detection rates are different, but they are consistent within the errors. Collecting a larger sample of 4.6 μm bright sources should allow us to decrease the errors and understand if the difference in detecting H I in absorption among obscured and unobscured AGN holds.

A different spin temperature could also be relevant to explain the lack of H I absorption in the stacking of the sources. In addition to the high T_{spin} characteristic of circumnuclear gas affected by the radiation from the AGN, the typical ISM has a large warm component. A number of studies (e.g. Maloney et al. 1996; Kanekar et al. 2003, 2009, 2011; Curran et al. 2007) have shown that in the typical ISM $N_{\mathrm{H\,I}} \sim 2 \times 10^{20}\ \mathrm{cm^{-2}}$ is the threshold column density for cold H I clouds ($T_{\mathrm{spin}} \lesssim 500$ K) and that lower column density H I has higher spin temperature ($T_{\mathrm{spin}} \gtrsim 600$ K). The undetected galaxies could be dominated by the low column density component, as the stacking of the ATLAS^{3D} galaxies suggests, implying that we observe mostly gas at high spin temperature. For a fixed column density, the optical depth decreases with increasing spin temperature. If in central regions of the non-detections most of the H I was warm, we would not have detected it in the stacking experiments of our survey.

4.3. Impact of the radio activity on the cold ISM of galaxies

In Figs. 4 and 5 we point out that among high-power sources ($\log P_{1.4\,\mathrm{GHz}} > 24\,\mathrm{W\,Hz^{-1}}$) 30% ± 15% have broad H I lines and that 36% ± 16% have lines that are shifted with respect to the systemic velocity. In Fig. 7 of G15 we show that among high-power sources the broadest lines are also more asymmetric and more blue-shifted with respect to the systemic velocity. We find very few cases of red-shifted absorption and they are all associated with relatively narrow lines. Furthermore, symmetric broad lines are detected only in interacting sources. All this seems to favour a scenario in which the unsettled kinematics of the H I we detect in absorption is due to an outflow driven by the nuclear activity, rather than a scenario in which the H I is unsettled prior to the triggering of the radio activity and may be falling into the radio source to contribute to its feeding. Nevertheless, cases of red-shifted narrow lines have been found, possibly in objects similar to NGC 315 (Morganti et al. 2009) and PKS B1718–649 (Maccagni et al. 2014).

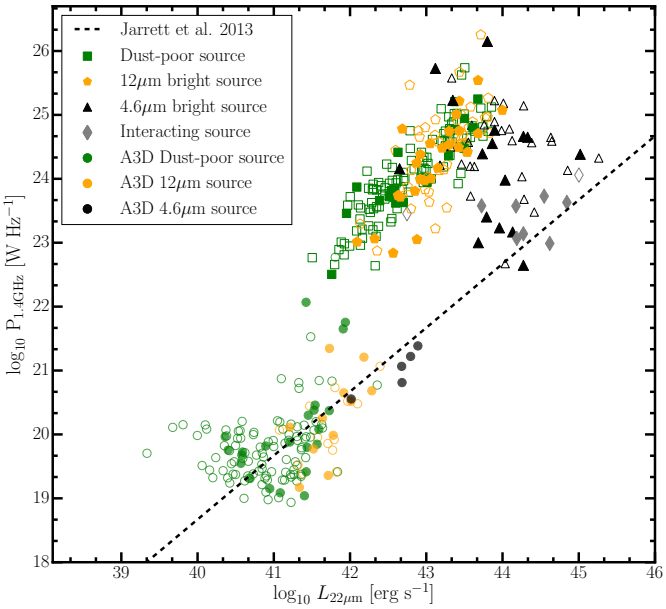

Fig. 9. Radio power of the sources vs. 22 μm luminosity for the sources of our sample and the ATLAS^{3D} sample (A3D), which have been observed in H I. The colour coding follows the WISE colour–colour plot shown in Fig. 1. The dashed line denotes the fit to the MIR-radio relation estimated by Jarrett et al. (2013).

In our sample, early-type radio sources rich in heated dust, i.e. MIR bright sources, have a higher detection rate in H I than dust-poor sources. Among high radio power sources, only MIR bright sources show broad lines. Figure 9 shows the MIR-radio relation ($\log P_{1.4\,\mathrm{GHz}}$ versus $\log_{10} L_{22\,\mu\mathrm{m}}$) for all sources in our sample and for the sources of the ATLAS^{3D} sample[3]. We also show a linear fit to the relation taken from the literature (Jarrett et al. 2013). The ATLAS^{3D} sample fits the relation well in the low star formation end. As expected, most sources in our sample are radio loud with respect to the relation. For the most powerful part of our sample ($\log P_{1.4\,\mathrm{GHz}} > 24\,\mathrm{W\,Hz^{-1}}$), the detection of broad, asymmetric lines (see Figs. 4 and 5) suggests that the energy released by the central AGN through the radio jets can perturb the circumnuclear cold gas. Among the galaxies of our sample that lie on the MIR-radio relation, H I is detected either in narrow lines, most likely tracing a disk, or in interacting sources. In these sources, the origin of the unsettled kinematics and of the star formation may be attributed to the interaction event itself.

The results of our survey are limited to AGN that were selected according to their radio flux. Mullaney et al. (2013) investigated the impact of the radio power of the sources on the circumnuclear ISM in an optically selected sample of AGN. These authors found that only AGN with radio power $\log_{10} P_{1.4\,\mathrm{GHz}} > 23\,\mathrm{W\,Hz^{-1}}$ show broad [OIII] lines and that compact radio cores play a major role in perturbing this gas, which is in agreement with the results of our study. Hence, it seems that AGN perturb the surrounding ISM mainly via the mechanical power of their

[3] We measure $L_{22\,\mu\mathrm{m}}$ from the magnitude found by WISE (W4).

Table 3. Summary of various upcoming H I 21 cm absorption line surveys.

Survey	Redshift [H I 21 cm]	Time per pointing [h]	Spectral r.m.s. [mJy]	Sky coverage [deg^2]	Total time [h]	Number of lines of sight
Apertif – SHARP	0–0.26	12	1.3	4000	6000	25 000 (>30 mJy)
ASKAP – FLASH	0.4–1.0	2	3.8	25 000	1600	65 000 (>90 mJy)
ASKAP – Wallaby	0–0.26	8	1.6	30 000	8000	132 000 (>40 mJy)
MeerKAT – MALS (*L*-band)	0–0.57	1.4	0.5	1300	1333	16 000 (>15 mJy)
MeerKAT – MALS (UHF-band)	0.40–1.44	1.7–2.8	0.5–0.7	2000	2125	33 000 (>15 mJy)

Notes. The two-part MALS project, MALS *L*-band, and MALS UHF are targeted surveys focussing on relatively bright, high redshift background sources to search the line of sight for intervening absorption. However, with the more than 1×1 deg^2 field of view of MeerKAT, a substantial volume for each pointing is blindly, and commensally, probed both for associated and intervening absorbers. SHARP and WALLABY are both commensal HI emission and absorption surveys, primarily investigating associated absorption. FLASH is a blind survey of the southern hemisphere to detect H I absorption in intervening and associated systems at intermediate redshifts ($z \sim 1$).

radio jets. In our sample, we see the effects of the radio jets expanding through the ISM in the ionised gas as well (Santoro et al., in prep). The major role played by the radio nuclear activity in perturbing the ISM is also suggested when looking at the H I in compact and extended radio sources. The former, where the radio jets have sub-galactic scales and are likely carving their way through its ISM, show broader and more offset lines than the latter, where the radio jets have already exited the galaxy; see Figs. 4 and 5 (left panels).

5. H I absorption detections in Apertif, ASKAP, and MeerKAT

The main results of our survey show the importance of H I absorption studies to trace the presence of cold gas in the central regions of early-type radio galaxies. Such studies allow us to understand how H I relates to the other components of the ISM, such as the warm dust, and how H I interacts with the nuclear radio emission. In particular, our survey shows that the detection rate of H I in absorption does not change in the range of redshifts and radio powers of the sample ($0.02 < z < 0.25$, $\log P_{1.4\,\mathrm{GHz}} = 22.5$ W Hz$^{-1} \lesssim \log P_{1.4\,\mathrm{GHz}} \lesssim 26.2$ W Hz^{-1}). Hence, H I absorption studies are the best tool to investigate the occurrence of H I in sources at all redshifts and radio powers.

The upcoming blind H I surveys of the SKA pathfinders and precursors, i.e. MeerKAT (Jonas 2009), the Australian SKA Pathfinder, (ASKAP, Johnston et al. 2008), and Apertif (Oosterloo et al. 2010b), will play a fundamental role in detecting H I in absorption, shed new light on its structure and its interplay with the radio nuclear activity, and they will be able to determine the occurrence of H I and its optical depth distribution down to low flux radio sources and intermediate redshift ($z \sim 1$).

In this section, we use the results of our survey to explore the possibilities for expanding this work in the upcoming H I surveys and to explore how the different surveys will cover the parameter space of radio sources and whether they will be complementary in describing the presence and properties of the H I.

A number of large area, wide bandwidth absorption line surveys are planned with next generation radio facilities. In Table 3 (Gupta, in prep.), we show the frequencies, redshift ranges, sky coverage, and flux limits of four of these surveys, which we consider in this section. In particular, we consider the survey from the new Apertif system on the WSRT, the Search for H I with Apertif (SHARP), the MeerKAT Absorption Line Survey (MALS) with the South African SKA precursor MeerKAT, and two surveys with the ASKAP facility, i.e. the Wide-field ASKAP *L*-band Legacy All-sky Blind surveY (WALLABY) and the First Large Absorption Survey in H I (FLASH). A dedicated, intermediate redshift survey, FLASH is searching for associated and intervening absorption at $0.5 < z < 1.0$. The WALLABY is a large sky coverage survey to detect H I in emission, which will also be sensitive to H I absorption at low redshifts. As with the survey presented in this paper, we focus in this section on the search for H I associated with the radio sources, although within the surveys, intervening absorption systems will also be investigated.

First, we simulate the continuum source population against which absorption will be seen. We combine the parameters of area, continuum sensitivity, and channel sensitivity of the survey (listed in Table 3) with a luminosity function from Mauch & Sadler (2007) and source number counts extracted from the simulations of Wilman et al. (2008). From this, we can determine the luminosity–redshift parameter space covered by the various planned surveys, shown in Fig. 10. The figure shows SHARP, MALS L band and MALS UHF, and the redshift ranges they cover. The WALLABY covers similar parameter space as SHARP, while FLASH and MALS UHF are both at higher redshift. The flux limits and channel sensitivities of the three surveys are well matched with each other, resulting in continuous coverage of the parameter space with large dynamic range at each redshift.

In Fig. 10, at low redshifts, SHARP in the northern hemisphere and WALLABY in the south cover very similar parameter space with WALLABY's larger volume containing more of the rare, high luminosity, low redshift objects. These are the only surveys probing low luminosity sources ($L < 10^{24}$ W Hz^{-1}).

At moderate redshifts, the MALS *L*-band survey is the only survey probing $0.26 < z < 0.42$, and will provide critical overlap with the intermediate redshift end of the MeerKAT deep HI emission surveys.

At intermediate redshifts ($z \sim 1$), MALS UHF and FLASH probe only the high luminosity sources, so care must be taken when comparing the absorption population at intermediate and low redshifts, as the continuum source populations are disparate

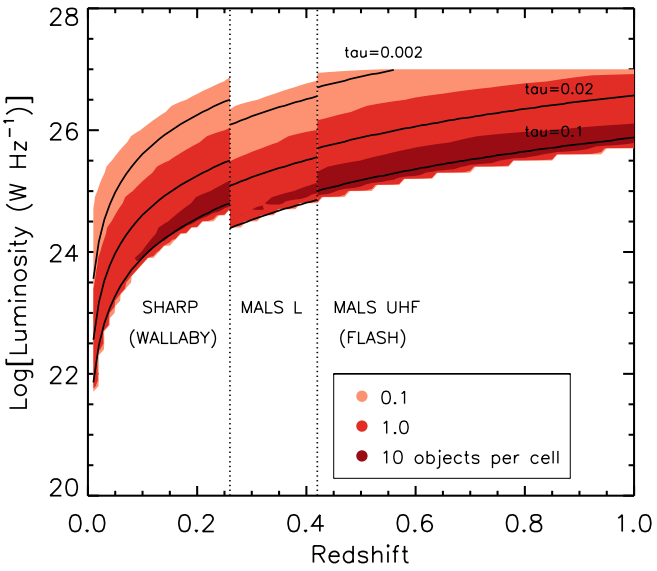

Fig. 10. Coverage of the luminosity–redshift plane by upcoming absorption surveys. The parameter space is divided into cells of dz = 0.01 and dL = 0.1, and the colour coding indicates 0.1 (light), 1 (medium), and 10 (dark shading) objects per cell. As expected, the majority of objects lie close to the flux limits of the surveys. At $z \leq 0.26$, SHARP in the northern hemisphere and WALLABY in the south cover very similar parameter space. The full MALS L-band survey covers $0 < z < 0.58$, but is the only survey probing intermediate redshifts, $0.26 < z < 0.42$. MALS UHF targets intermediate redshifts, $0.42 < z < 1$. A similar redshift range is covered by FLASH, but with brighter flux limits. For clarity, we show the coverage of the plane out to $z = 1$, even though both surveys extend to $z = 1.44$ with the same behaviour. The black lines denote the minimum optical depth visible for sources of a given flux with the channel rms values given in Table 3.

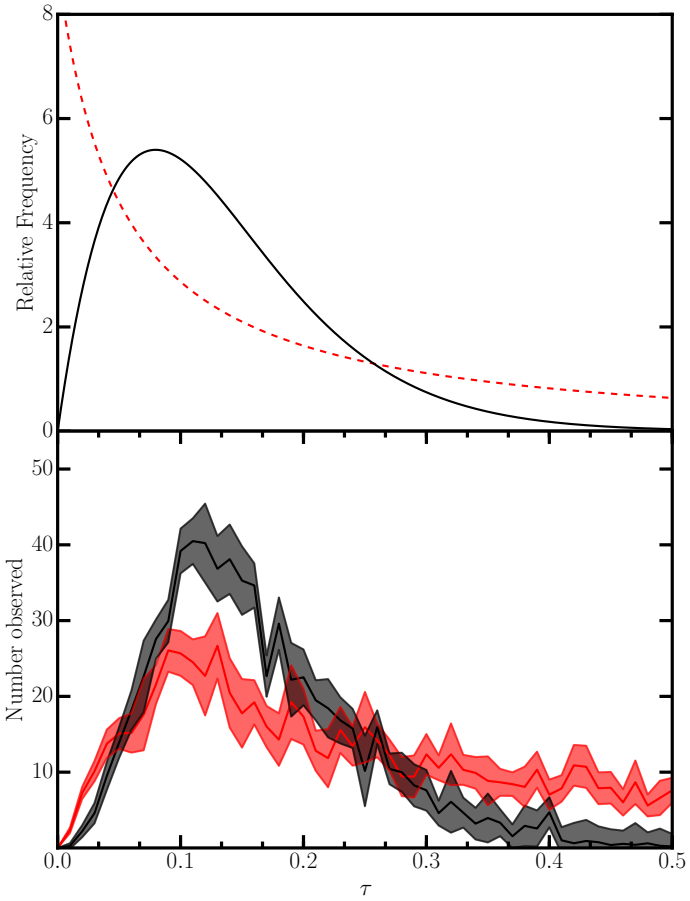

Fig. 11. *Top panel*: two suggested intrinsic distributions for the frequency of associated absorbers of a given optical depth. The primary difference is at very low optical depth values, where the exponential-shaped distribution is dominated by low values, whereas the other peaks at $\tau \sim 0.08$. *Bottom panel*: resulting observed optical depth distributions for the SHARP survey, assuming absorbers are drawn from the two distributions in the *top panel*. The solid lines indicate the average observed distributions, while the shaded regions their dispersion.

and, as we have seen here, the H I can have different properties in different types of radio sources. The relatively bright flux limit of FLASH restricts the dynamic range in continuum sources, but the large area will result in excellent statistics of both intervening and associated absorbers, enabling evolution in the absorber population to be probed.

After determining the distribution of continuum sources available for each survey, we add the absorption population. We assume that one out of three sources will have an associated absorber, regardless of the source flux or range of observable absorber depths. Figure 10 shows that for each source and survey channel sensitivity, there is a minimum peak optical depth value that is observable. In the figure, we denote three minimum observable peak optical depths with black lines ($\tau \sim 0.1$, $\tau \sim 0.02$, and $\tau \sim 0.002$).

Figure 10 shows that the different surveys complement each other. In high-power radio sources ($\log P_{1.4\,\mathrm{GHz}} \gtrsim 10^{25}$ W Hz^{-1}), these surveys will allow us to detect HI at $0.002 < \tau < 0.1$ to $z \lesssim 0.5$, and $\tau > 0.02$ to $z \lesssim 1$. Hence, in powerful radio sources we will be able to trace the evolution of the properties of H I with redshift. However, the bulk of the population of radio sources has low radio power and its H I absorption content will be explored only by the low redshift surveys, for example the extension of the research presented in this paper.

In the survey presented in this paper, we find a dichotomy in the detection of H I, suggesting the gas has high optical depth in the detections and very low optical depth in the non-detections. From this, we assume two different distributions to model the (unknown) intrinsic absorption population (see the top panel of Fig. 11) and to extract the distribution we expect to observe with the SHARP survey. The exponential shape might naively be expected, since the most common, low column density H I clouds correspond to very low optical depth absorption. On the contrary, the second shape, which is modelled on a black-body curve, has very few low optical depth absorbers while maintaining large number of absorbers with moderate optical depth. For one out of three sources, an absorber of a given optical depth is chosen randomly from the visible τ values, separately for the two intrinsic distributions. No redshift evolution in the absorber population is included.

The bottom panel of Fig. 11 shows the results of this exercise for the SHARP survey. The resulting observed distributions are sufficiently different and upcoming surveys should be able to constrain the intrinsic distribution from which the absorbers are drawn. The observed optical depth distribution is a convolution of the galaxy luminosity function and the intrinsic optical depth distribution. Its shape depends from the fact that most of the observed objects are assigned values of $\tau \geq 0.1$ and are close to the flux limit of the observations. Thus, aside from the normalisation, within this simplistic simulation the shapes of the observed distributions from survey to survey are similar.

The targeted aspect of MALS, with deep integrations of bright sources, will help fill in the very low τ values.

Some evolution of the absorption population is expected and this should be seen in the optical depth distribution observed in the intermediate redshift sources. Also, the occurrence of absorption as a function of optical depth and continuum flux will be better determined from uniform, blind surveys, which provide information about the distribution of the absorbing gas in galaxies.

Interestingly, the lack of absorption seen so far in the stacking exercises indicates that very low optical depth values are not common and this disfavours the exponential underlying optical depth distribution. Larger samples of uniformly selected and observed objects will strengthen this restriction.

6. Concluding remarks

In this paper, we presented new WSRT observations of 147 radio sources (30 mJy $< S_{1.4\,\mathrm{GHz}} <$ 50 mJy, $0.02 < z < 0.25$) observed in search for H I absorption. We detected H I in 34 sources (see Appendix A). We combined this sample with the sample of 101 sources with $S_{1.4\,\mathrm{GHz}} > 50$ mJy, observed in a similar way and presented in G14 and G15. We classified the 248 sources of the sample according to their radio continuum emission (compact sources and extended sources) and to their WISE colours (dust-poor, 12 μm bright, and 4.6 μm bright sources; see Sect. 2.2). The vast majority of the sample lies above the MIR-radio relation, suggesting the bulk of their radio emission comes from the central AGN (see Sect. 4.3). We analysed the occurrence, distribution, and kinematics of the H I with the following results:

- Twenty-seven percent of radio-galaxies have H I detected in absorption associated with the source. The detection rate does not vary across the range of redshifts and radio powers of the sample (see Sect. 3.1).
- AGN with radio-power $\log P_{1.4\,\mathrm{GHz}} < 24$ W Hz^{-1} only show narrow H I absorption lines. Broad lines, which can trace a significant component of H I unsettled by the radio activity, are found only in powerful radio AGN ($\log P_{1.4\,\mathrm{GHz}} > 24$ W Hz^{-1}).
- Compact sources show broad lines, tracing H I with unsettled kinematics. Compact sources also show a higher detection rate of H I than extended sources.
- Dust-poor galaxies, at all radio powers, show only narrow and deep H I absorption lines (see Fig. 6), mostly centred at the systemic velocity, suggesting that in these galaxies most of the H I is settled in a rotating disk.
- In MIR bright sources we detect H I more often than in dust-poor sources. Above $\log P_{1.4\,\mathrm{GHz}} > 24$ W Hz^{-1}, these sources often show broad lines, suggesting the H I has unsettled kinematics.
- Three of the most powerful MIR bright sources show broad ($FWHM > 300$ km s^{-1}) H I lines with a blue-shifted wing. These lines are likely to trace an outflow of neutral hydrogen pushed out of the galaxy by the radio jets.
- The broad and asymmetric H I lines we detect all have a blue-shifted wing, while broad lines with a red-shifted component are not found. This may favour a scenario in which the kinematics of the H I are unsettled by the expansion of the nuclear activity, i.e. an outflow, rather than a scenario in which the H I is unsettled prior to the triggering of the radio activity and may be falling into the radio source.
- Stacking experiments on the non-detections of our sample do not reveal a detection of H I absorption. In stacking the subgroups of sources where the detection rate of H I is higher, i.e. compact sources and MIR bright sources, we still do not detect any absorption line (see Sect. 3.3).
- As reference, we stack the non-detections of the ATLAS^{3D} sample (Serra et al. 2012); we detect an H I emission line with $\sim 3\sigma$ significance, tracing H I with very low column density $N_{\mathrm{H\,I}} \sim 2.1 \times 10^{19}$ cm^{-2}. If all this H I was cold ($T_{\mathrm{spin}} \lesssim 100$ K), the corresponding optical depth would be three times lower than the detection limit of our stacking experiment in absorption (see Table 2). If the H I was warmer, the optical depth would be even lower. Given that the H I has much higher optical depths when is directly detected, this suggests a bi-modality in the occurrence of H I in early-type galaxies. Of these galaxies, 27% ± 5.5% have H I, detectable in absorption with short targeted observations (4–6 h). The other galaxies, if they are not completely depleted of it, have H I at very low column densities or higher spin temperatures.
- Orientation effects do not seem to be the only explanation as to why H I is detected (or not) in absorption. There are suggestions that orientation effects may be important in particular subsamples of sources, such as powerful radio sources where the host galaxy is edge-on and 4.6 μm bright sources. However, these results are affected by the small number of sources of these subsamples.
- The upcoming H I absorption surveys of the SKA pathfinders (SHARP with Apertif, MALS with MeerKAT, and FLASH with ASKAP) will allow us to probe the H I optical depth distribution for radio sources out to redshift $z \sim 1$. The three surveys are complementary in the redshift intervals, and only the combination of all three will allow us to investigate the H I content in radio sources of all radio powers and at all redshifts. In particular, SHARP and WALLABY are the only surveys which, at low redshifts ($z \lesssim 0.26$), will allow us to probe the entire range of radio powers, 22 W Hz^{-1} $< \log_{10} P_{1.4\mathrm{GHz}} <$ 26 W Hz^{-1}.

Acknowledgements. The WSRT is operated by the ASTRON (Netherlands Foundation for Research in Astronomy) with support from the Netherlands Foundation for Scientific Research (NWO). This research makes use of the SDSS Archive, funding for the creation and distribution of which was provided by the Alfred P. Sloan Foundation, the Participating Institutions, the National Aeronautics and Space Administration, the National Science Foundation, the US Department of Energy, the Japanese Monbukagakusho, and the Max Planck Society. This publication makes use of data products from the Wide-field Infrared Survey Explorer, which is a joint project of the University of California, Los Angeles, and the Jet Propulsion Laboratory/California Institute of Technology, funded by the National Aeronautics and Space Administration. For this research we made extensive use of the software Karma (Gooch 1996) and TOPCAT (Taylor 2005). The research leading to these results has received funding from the European Research Council under the European Union's Seventh Framework Programme (FP/2007–2013)/ERC Advanced Grant RADIOLIFE-320745. The authors wish to thank Dr. Robert Schulz and Dr. Bradley Frank for useful discussions and suggestions.

References

Alatalo, K., Blitz, L., Davis, T. A., et al. 2011, ApJ, 735, 88
Allison, J. R., Curran, S. J., Emonts, B. H. C., et al. 2012, MNRAS, 423, 2601
Allison, J. R., Sadler, E. M., & Meekin, A. M. 2014, MNRAS, 440, 696
Allison, J. R., Sadler, E. M., Moss, V. A., et al. 2015, MNRAS, 453, 1249
Bahcall, J. N., Kirhakos, S., Saxe, D. H., & Schneider, D. P. 1997, ApJ, 479, 642
Becker, R. H., White, R. L., & Helfand, D. J. 1995, ApJ, 450, 559
Best, P. N., Kauffmann, G., Heckman, T. M., & Ivezić, Ž. 2005, MNRAS, 362, 9
Beswick, R. J., Pedlar, A., & Holloway, A. J. 2002, MNRAS, 329, 620
Beswick, R. J., Peck, A. B., Taylor, G. B., & Giovannini, G. 2004, MNRAS, 352, 49

Bower, R. G., Benson, A. J., Malbon, R., et al. 2006, MNRAS, 370, 645
Cappellari, M., Emsellem, E., Krajnović, D., et al. 2011, MNRAS, 413, 813
Chandola, Y., & Saikia, D. J. 2017, MNRAS, 465, 997
Chandola, Y., Gupta, N., & Saikia, D. J. 2013, MNRAS, 429, 2380
Ciotti, L., Ostriker, J. P., & Proga, D. 2010, ApJ, 717, 708
Cluver, M. E., Jarrett, T. H., Hopkins, A. M., et al. 2014, ApJ, 782, 90
Conway, J. E., & Blanco, P. R. 1995, ApJ, 449, L131
Crenshaw, D. M., Kraemer, S. B., Hutchings, J. B., et al. 2000, AJ, 120, 1731
Curran, S. J., Tzanavaris, P., Pihlström, Y. M., & Webb, J. K. 2007, MNRAS, 382, 1331
Curran, S. J., Whiting, M. T., Murphy, M. T., et al. 2011, MNRAS, 413, 1165
Curran, S. J., Allison, J. R., Glowacki, M., Whiting, M. T., & Sadler, E. M. 2013a, MNRAS, 431, 3408
Curran, S. J., Whiting, M. T., Tanna, A., et al. 2013b, MNRAS, 429, 3402
Curran, S. J., Whiting, M. T., Allison, J. R., et al. 2017, MNRAS, 467, 4514
Dasyra, K. M., & Combes, F. 2011, A&A, 533, L10
den Heijer, M., Oosterloo, T. A., Serra, P., et al. 2015, A&A, 581, A98
Emonts, B. H. C., Morganti, R., Struve, C., et al. 2010, MNRAS, 406, 4987
Fabian, A. 2012, ARA&A, 50, 455
Fanti, C. 2009, Astron. Nachr., 330, 120
Fanti, C., Fanti, R., Dallacasa, D., et al. 1995, A&A, 302, 317
Faucher-Giguère, C.-A., & Quataert, E. 2012, MNRAS, 425, 605
Faucher-Giguere, C.-A., Quataert, E., & Hopkins, P. F. 2013, MNRAS, 433, 1970
Feruglio, C., Maiolino, R., Piconcelli, E., et al. 2010, A&A, 518, L155
Fischer, T. C., Crenshaw, D. M., Kraemer, S. B., Schmitt, H. R., & Turner, T. J. 2014, ApJ, 785, 25
García-Burillo, S., Combes, F., Schinnerer, E., Boone, F., & Hunt, L. K. 2005, A&A, 441, 1011
Geréb, K., Morganti, R., & Oosterloo, T. A. 2014, A&A, 569, A35
Geréb, K., Maccagni, F. M., Morganti, R., et al. 2015, A&A, 575, A44
Glowacki, M., Allison, J. R., Sadler, E. M., et al. 2017, MNRAS, 467, 2766
Gooch, R. 1996, Astronomical Data Analysis Software and Systems V, ASP Conf. Ser., 101, 80
Guillard, P., Ogle, P., Emonts, B., et al. 2012, ApJ, 747, 95
Gupta, N., Salter, C. J., Saikia, D. J., Ghosh, T., & Jeyakumar, S. 2006, MNRAS, 373, 972
Holt, J., Tadhunter, C. N., & Morganti, R. 2003, MNRAS, 342, 227
Holt, J., Tadhunter, C. N., & Morganti, R. 2008, MNRAS, 387, 639
Jackson, N., Beswick, R., Pedlar, A., et al. 2003, MNRAS, 338, 643
Jarrett, T. H., Masci, F., Tsai, C. W., et al. 2013, AJ, 145, 6
Johnston, S., Taylor, R., Bailes, M., et al. 2008, Exp. Astron., 22, 151
Jonas, J. 2009, Proc. IEEE, 97, 1522
Kanekar, N., & Chengalur, J. N. 2008, MNRAS, 384, L6
Kanekar, N., Subrahmanyan, R., Chengalur, J. N., & Safouris, V. 2003, MNRAS, 346, L57
Kanekar, N., Smette, A., Briggs, F. H., & Chengalur, J. N. 2009, ApJ, 705, L40
Kanekar, N., Braun, R., & Roy, N. 2011, ApJ, 737, L33
King, A., & Nixon, C. 2015, MNRAS, 453, L46
King, A., & Pounds, K. 2015, ARA&A, 53, 115
Labiano, A. 2008, A&A, 488, L59
Lee, J. C., Hwang, H. S., & Ko, J. 2013, ApJ, 774, 62
Lehnert, M. D., Tasse, C., Nesvadba, N. P. H., Best, P. N., & van Driel, W. 2011, A&A, 532, L3
Maccagni, F. M., Morganti, R., Oosterloo, T. A., & Mahony, E. K. 2014, A&A, 571, A67
Maccagni, F. M., Santoro, F., Morganti, R., et al. 2016, A&A, 588, A46
Mahony, E. K., Morganti, R., Emonts, B. H. C., Oosterloo, T. A., & Tadhunter, C. 2013, MNRAS, 435, L58
Mahony, E. K., Oonk, J. B. R., Morganti, R., et al. 2016, MNRAS, 455, 2453
Maloney, P. R., Hollenbach, D. J., & Tielens, A. G. G. M. 1996, ApJ, 466, 561
Mauch, T., & Sadler, E. M. 2007, MNRAS, 375, 931
McNamara, B., & Nulsen, P. 2007, ARA&A, 45, 117
Mingo, B., Watson, M. G., Rosen, S. R., et al. 2016, MNRAS, 462, 2631
Morganti, R., Oosterloo, T. A., Tadhunter, C. N., et al. 2001, MNRAS, 323, 331
Morganti, R., Oosterloo, T. A., Tadhunter, C. N., van Moorsel, G., & Emonts, B. 2005a, A&A, 439, 521
Morganti, R., Tadhunter, C. N., & Oosterloo, T. A. 2005b, A&A, 444, L9
Morganti, R., De Zeeuw, P. T., Oosterloo, T. A., et al. 2006, MNRAS, 371, 157
Morganti, R., Peck, A. B., Oosterloo, T. A., et al. 2009, A&A, 505, 559
Morganti, R., Fogasy, J., Paragi, Z., Oosterloo, T., & Orienti, M. 2013a, Sciences, 341, 1082
Morganti, R., Frieswijk, W., Oonk, R. J. B., Oosterloo, T., & Tadhunter, C. 2013b, A&A, 552, L4
Morganti, R., Oosterloo, T., Raymond Oonk, J. B., Frieswijk, W., & Tadhunter, C. 2015, A&A, 580, A1
Morganti, R., Veilleux, S., Oosterloo, T., Teng, S. H., & Rupke, D. 2016, A&A, 593, A30
Mullaney, J. R., Alexander, D. M., Fine, S., et al. 2013, MNRAS, 433, 622
Murgia, M. 2003, PASA, 20, 19
Nyland, K., Young, L. M., Wrobel, J. M., et al. 2017, MNRAS, 464, 1029
Ochsenbein, F., Bauer, P., & Marcout, J. 2000, A&AS, 143, 23
O'Dea, C. P. 1998, PASP, 110, 493
Oosterloo, T. A., Morganti, R., Tzioumis, A., et al. 2000, AJ, 119, 2085
Oosterloo, T., Morganti, R., Crocker, A., et al. 2010a, MNRAS, 409, 500
Oosterloo, T., Verheijen, M., & van Cappellen, W. 2010b, The latest on Apertif, PoS (SKAF2010) 043
Orienti, M. 2016, Astron. Nachr., 337, 9
Pihlström, Y. M., Conway, J. E., & Vermeulen, R. C. 2003, A&A, 404, 871
Readhead, A. C. S., Taylor, G. B., Xu, W., et al. 1996, ApJ, 460, 612
Reeves, J. N., Sambruna, R. M., Braito, V., & Eracleous, M. 2009, ApJ, 702, L187
Rosario, D. J., Burtscher, L., Davies, R., et al. 2013, ApJ, 778, 94
Rose, M., Elvis, M., Crenshaw, M., & Glidden, A. 2015, MNRAS, 451, L11
Sadler, E. M. 2016, Astron. Nachr., 337, 105
Sadler, E. M., Cannon, R. D., Mauch, T., et al. 2007, MNRAS, 381, 211
Sault, R., Teuben, P., & Wright, M. 1995, ASP Conf. Ser., 77, 433
Serra, P., Oosterloo, T., Morganti, R., et al. 2012, MNRAS, 422, 1835
Serra, P., Oser, L., Krajnovi, D., et al. 2014, MNRAS, 444, 3388
Silk, J., & Rees, M. J. 1998, A&A, 331, L1
Stern, D., Assef, R. J., Benford, D. J., et al. 2012, ApJ, 753, 30
Struve, C., & Conway, J. E. 2010, A&A, 513, A10
Struve, C., & Conway, J. E. 2012, A&A, 546, A22
Struve, C., Oosterloo, T. A., Morganti, R., & Saripalli, L. 2010, A&A, 515, A67
Tadhunter, C. N., Villar-Martin, M., Morganti, R., Bland-Hawthorn, J., & Axon, D. 2000, MNRAS, 314, 849
Taylor, M. B. 2005, ASP Conf. Ser., 347, 29
van der Hulst, J. M., Golisch, W. F., & Haschick, A. D. 1983, ApJ, 264, L37
van Gorkom, J. H., Knapp, G. R., Ekers, R. D., et al. 1989, AJ, 97, 708
Vermeulen, R. C., Pihlström, Y. M., Tschager, W., et al. 2003, A&A, 404, 861
Westmeier, T., Jurek, R., Obreschkow, D., Koribalski, B. S., & Staveley-Smith, L. 2014, MNRAS, 438, 1176
Wilman, R. J., Miller, L., Jarvis, M. J., et al. 2008, MNRAS, 388, 1335
Wright, E. L., Eisenhardt, P. R. M., Mainzer, A. K., et al. 2010, AJ, 140, 1868
York, D. G., Adelman, J., Anderson, Jr., J. E., et al. 2000, AJ, 120, 1579

Appendix A: Ancillary information on the sample

Here, we show the 34 H I absorption lines detected with the WSRT from observations between December 2013 and February 2015 in radio sources with 30 mJy $< S_{1.4\,\mathrm{GHz}} <$ 50 mJy. In Table A.1 we show the main properties of the sources and the parameters of the detected lines measured using the busy function.

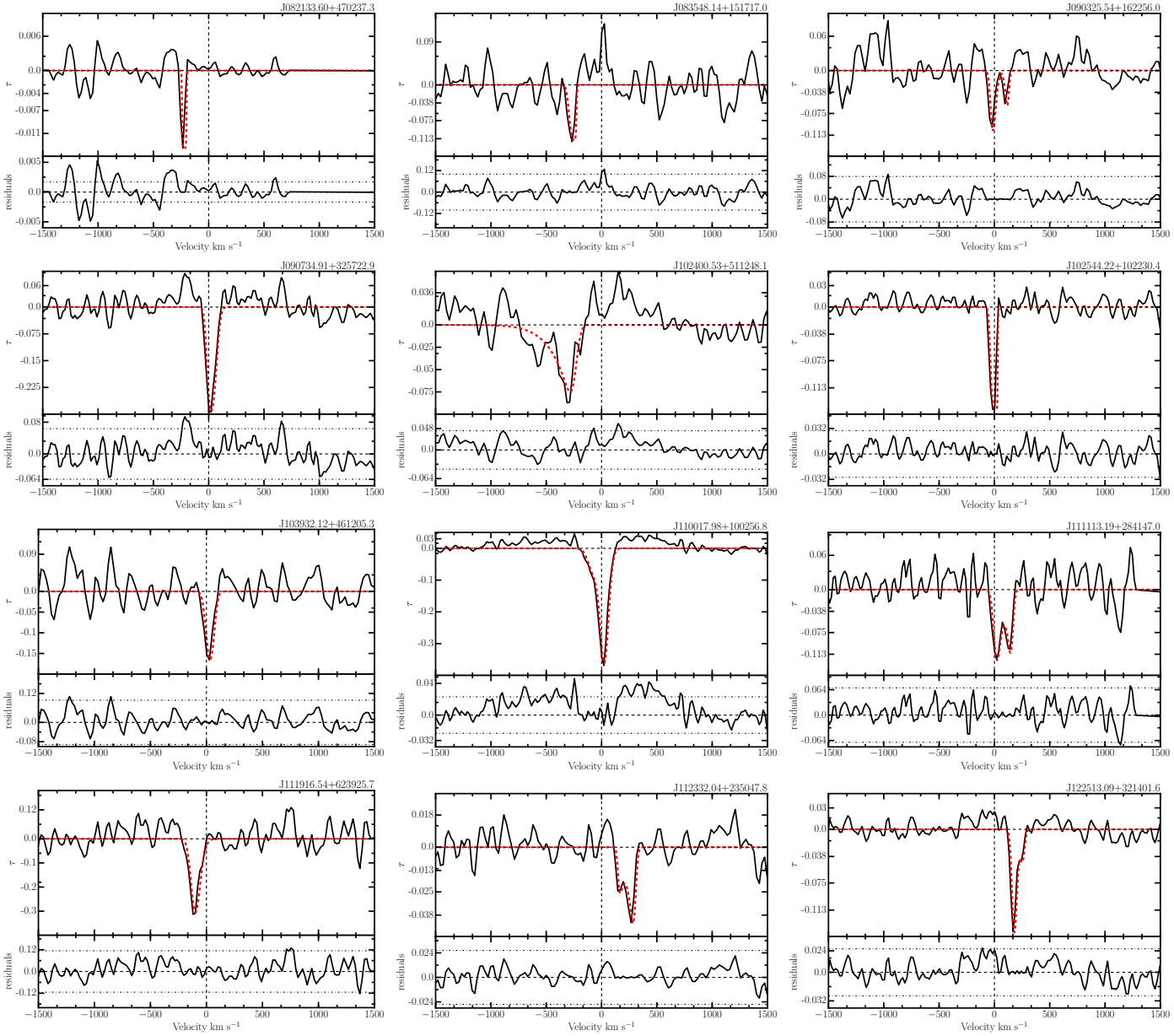

Fig. A.1. H I absorption detections. The data are shown in black, the BF fit is shown in red. The residuals of the fit are plotted in the *bottom panels* along with the $\pm 3\sigma$ noise level (horizontal dotted lines).

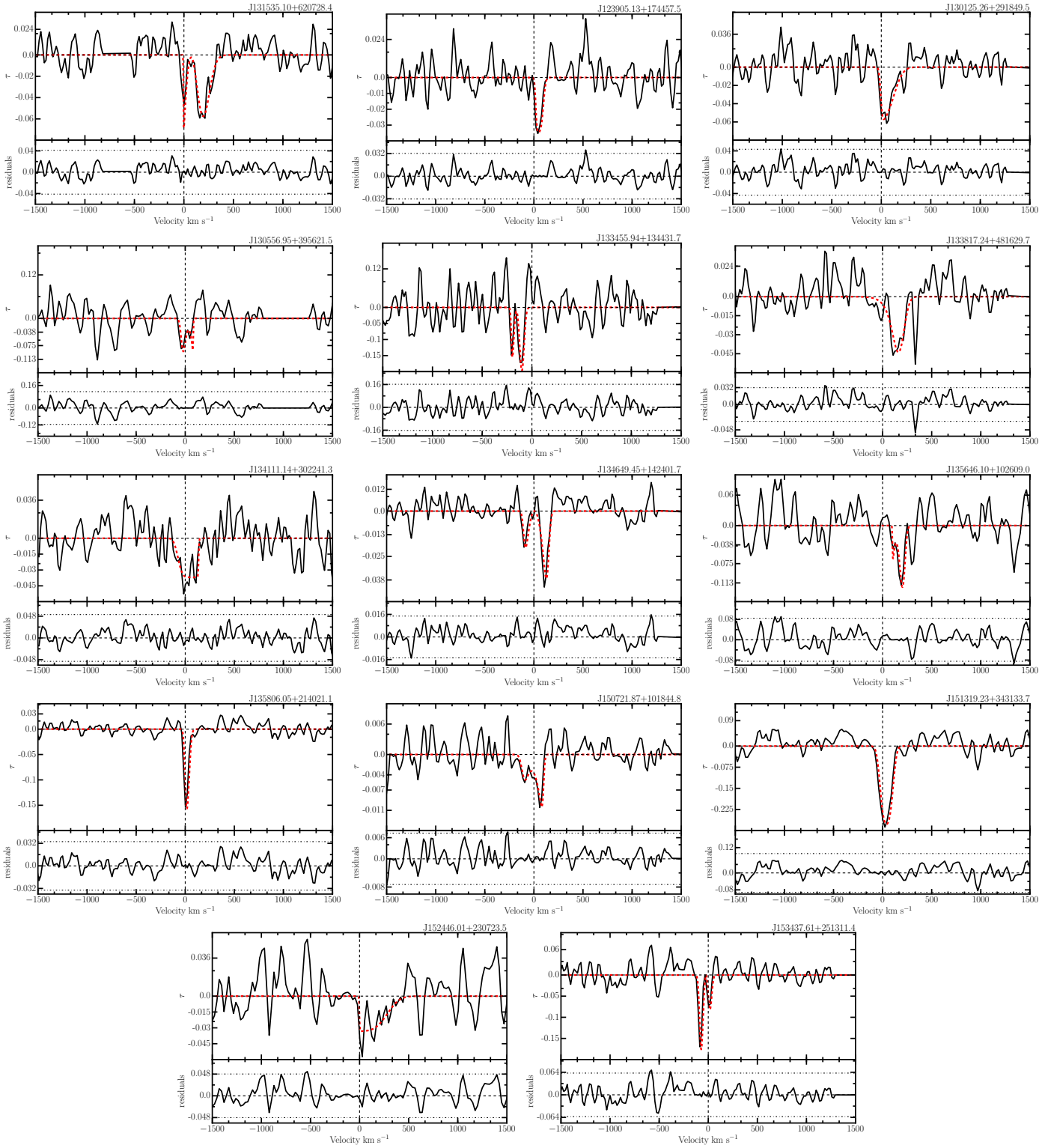

Fig. A.1. continued.

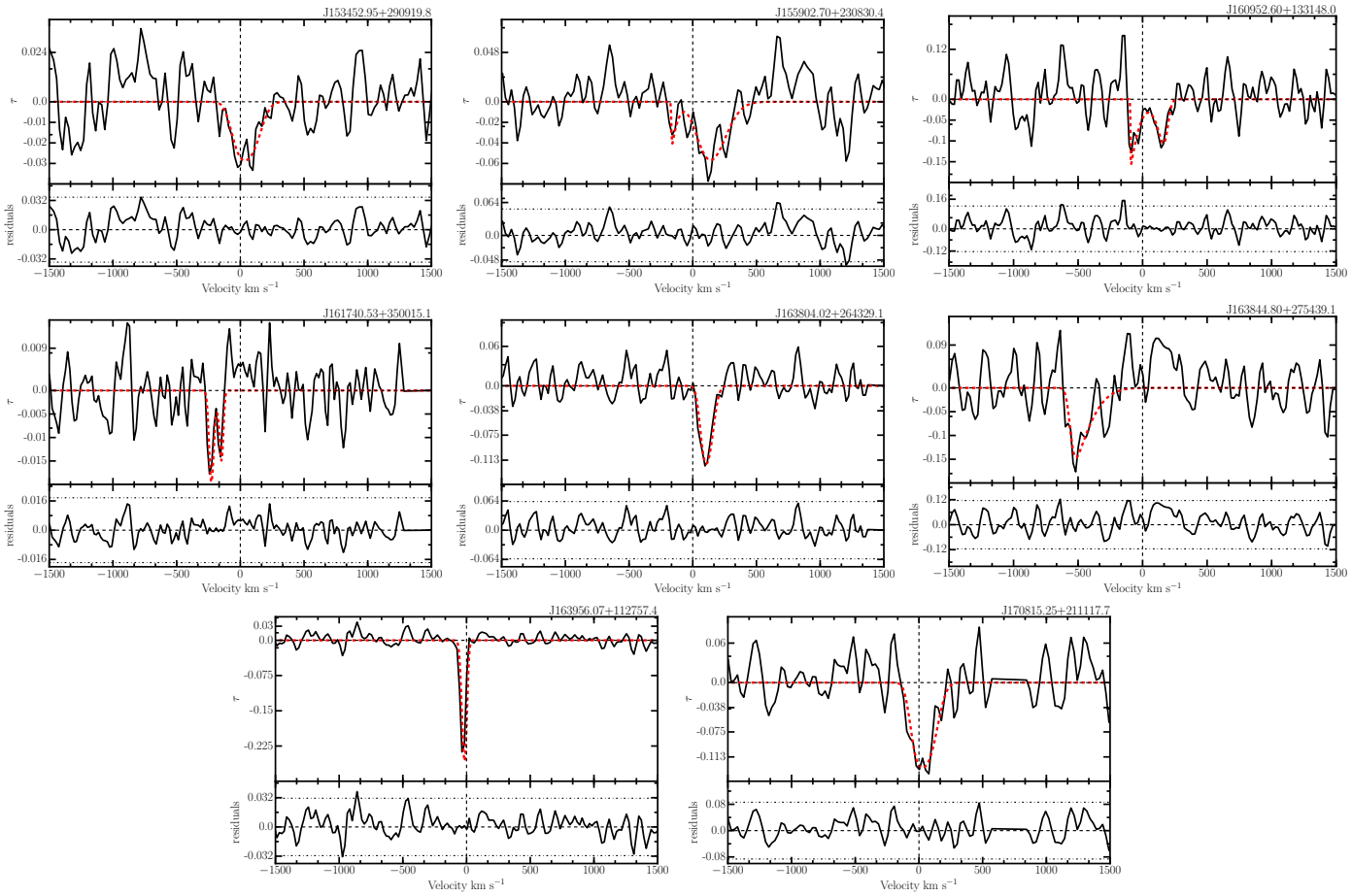

Fig. A.1. continued.

Table A.1. Table of sources.

Source J2000	z_{opt}	$S_{1.4\ GHz}$ [mJy]	$P_{1.4\ GHz}$ [W Hz^{-1}]	Radio type [C/E/I]	WISE type (6)	Noise (3σ) [mJy]	τ_{peak}	$\int \tau\, dv$ [km s^{-1}]	FWHM [km s^{-1}]	FW20 [km s^{-1}]	Centroid [km s^{-1}]
J075157.32+522309.2	0.1887	68.47	24.84	C	4.6 μm	<2.47	–	–	–	–	–
J075244.19+455657.4	0.0517	55.54	23.55	I	12 μm	<1.85	–	–	–	–	–
J075555.12+420756.7	0.15	57.56	24.54	I	12 μm	<5.58	–	–	–	–	–
J075607.06+383401.0*	0.2156	70.18	24.98	C	dp	<2.82	–	–	–	–	–
J075648.71+531256.2	0.0837	39.15	23.83	C	dp	<1.78	–	–	–	–	–
J075756.71+395936.1*	0.0658	91.27	23.98	C	4.6 μm	1.85	0.042	5.96	122.52 ± 14.7	244.68 ± 15.66	−22.49 ± 5.73
J075828.10+374711.8*	0.0408	243.0	23.98	I	dp	<2.18	–	–	–	–	–
J075846.99+270515.6*	0.0987	69.05	24.23	C	4.6 μm	<3.76	–	–	–	–	–
J075940.96+505023.9	0.0544	42.91	23.48	C	4.6 μm	<1.64	–	–	–	–	–
J080041.98+321727.6*	0.1872	104.0	25.01	C	dp	<2.47	–	–	–	–	–
J080601.51+190614.7*	0.0979	142.0	24.54	I	12 μm	3.08	0.099	18.17	189.89 ± 9.44	266.22 ± 9.54	104.05 ± 4.53
J080624.94+172503.7	0.1041	37.44	24.01	I	dp	<2.65	–	–	–	–	–
J080938.88+345537.2*	0.0825	142.32	24.38	I	12 μm	1.24	0.009	0.71	82.4 ± 24.39	108.15 ± 25.7	−243.29 ± 9.15
J081040.29+481233.1	0.0775	73.18	24.03	C	4.6 μm	<5.88	–	–	–	–	–
J081601.88+380415.4	0.1727	67.86	24.75	I	dp	<2.99	–	–	–	–	–
J081827.34+281402.8*	0.2252	46.63	24.84	C	4.6 μm	<2.14	–	–	–	–	–
J081854.09+224744.8*	0.0958	194.0	24.65	I	12 μm	<2.12	–	–	–	–	–
J082028.10+485347.4*	0.1324	124.0	24.76	I	dp	<3.18	–	–	–	–	–
J082133.60+470237.3	0.128	1239.99	25.73	I	4.6 μm	2.1	0.0038	0.56	41.47 ± 3.33	47.24 ± 4.35	−254.33 ± 12.0
J082209.54+470552.9	0.1271	54.95	24.37	C	dp	<2.94	–	–	–	–	–
J082440.14+410305.6	0.058	75.93	23.79	I	dp	<2.62	–	–	–	–	–
J082814.20+415351.9	0.226	84.47	25.11	I	dp	<2.57	–	–	–	–	–
J082904.82+175415.8*	0.0895	190.0	24.58	I	12 μm	<2.27	–	–	–	–	–
J083138.83+223422.9*	0.0869	92.56	24.24	I	dp	<2.01	–	–	–	–	–
J083139.79+460800.8*	0.1311	123.0	24.75	C	dp	<2.68	–	–	–	–	–
J083411.09+580321.4*	0.0934	46.31	24.01	C	dp	<2.57	–	–	–	–	–
J083548.14+151717.0	0.1684	45.48	24.55	I	4.6 μm	4.5	0.1133	8.05	67.56 ± 11.58	86.05 ± 15.0	−289.36 ± 31.74
J083637.84+440109.6*	0.0554	134.0	23.99	C	12 μm	1.93	0.016	1.37	77.92 ± 17.38	206.4 ± 26.8	25.67 ± 13.27
J083903.08+401545.6	0.1941	40.06	24.63	I	dp	<1.96	–	–	–	–	–
J083915.82+285038.7*	0.079	126.0	24.29	I	dp	<2.86	–	–	–	–	–
J084307.11+453742.8*	0.1919	331.0	25.54	C	12 μm	5.8	0.273	25.86	79.16 ± 37.17	126.75 ± 19.98	57.85 ± 59.03
J084359.13+510524.9*	0.1263	79.03	24.52	I	dp	<3.17	–	–	–	–	–
J084522.15+112550.4	0.0662	159.87	24.23	I	dp	<3.72	–	–	–	–	–
J084712.92+113350.1	0.1984	32.97	24.57	C	4.6 μm	<4.44	–	–	–	–	–
J090100.09+103701.7	0.0295	45.96	22.96	I	dp	<2.35	–	–	–	–	–
J090105.25+290146.9*	0.194	1670.0	26.25	I	12 μm	<1.67	–	–	–	–	–
J090206.46+203037.6	0.0815	57.02	23.97	I	dp	<1.87	–	–	–	–	–
J090209.87+283042.9	0.0849	34.61	23.79	C	dp	<1.82	–	–	–	–	–
J090325.54+162256.0	0.1823	47.81	24.65	C	4.6 μm	3.75	0.0949	8.98	163.02 ± 43.22	187.67 ± 41.56	2.97 ± 36.58
J091039.92+184147.7	0.0284	48.09	22.95	I	dp	<3.0	–	–	–	–	–
J091218.36+483045.1*	0.1172	143.14	24.71	I	dp	<3.95	–	–	–	–	–
J091651.94+523828.3*	0.1904	63.01	24.81	I	dp	<3.31	–	–	–	–	–

Notes. Column (1): J2000 coordinates of the sources; (2) redshift measured from the SDSS spectrum; (3) flux at 1.4 GHz; (4) radio power; (5) radio classification as compact (C), extended (E) and interacting (I) sources; (6) WISE colour–colour classification as dust poor (dp), 12 μm bright (12 μm) and 4.6 μm bright (4.6 μm) galaxies (see Sect. 2.2); (7) 3σ detection limit of the H I spectrum; (8) peak optical depth of the H I detections; (9) full width at half maximum; (10) full width at 20% of the peak flux; (11) position of the centroid of the line. Galaxies denoted by (*) have been presented in G14 and G15.

Table A.1. continued.

Source J2000	z_{opt}	$S_{1.4\ GHz}$ [mJy]	$P_{1.4\ GHz}$ [W Hz^{-1}]	Radio type [C/E/I]	WISE type (6)	Noise (3σ) [mJy]	τ_{peak}	$\int \tau\, dv$ [km s^{-1}]	FWHM [km s^{-1}]	FW20 [km s^{-1}]	Centroid [km s^{-1}]
J092151.49+332406.7	0.0236	51.16	22.81	I	dp	<1.83	–	–	–	–	–
J092405.30+141021.4	0.1356	120.01	24.77	C	dp	<4.41	–	–	–	–	–
J092445.88+304933.0	0.2118	42.32	24.74	I	dp	<4.71	–	–	–	–	–
J092511.57+190713.1	0.1291	38.23	24.22	C	12 μm	<3.09	–	–	–	–	–
J092740.64+554548.0	0.221	64.18	24.96	I	12 μm	<2.45	–	–	–	–	–
J093004.05+341326.5	0.0421	30.43	23.1	C	dp	<1.52	–	–	–	–	–
J093414.30+241335.1	0.0504	30.55	23.26	C	dp	<1.79	–	–	–	–	–
J093551.59+612111.3*	0.0394	148.0	23.73	2.0	4.6 μm	1.82	0.073	33.08	536.43 ± 9.97	825.84 ± 10.68	−78.08 ± 4.49
J093609.36+331308.3*	0.0762	60.63	23.94	C	dp	<1.79	–	–	–	–	–
J094319.15+361452.1*	0.0223	104.0	23.07	C	dp	<1.86	–	–	–	–	–
J094521.33+173753.2	0.1281	49.02	24.33	I	4.6 μm	<3.06	–	–	–	–	–
J094542.23+575747.7*	0.2289	89.3	25.14	C	4.6 μm	<2.64	–	–	–	–	–
J100935.70+182601.5*	0.1165	43.7	24.19	I	dp	<3.68	–	–	–	–	–
J101256.03+163853.0	0.118	37.56	24.13	C	4.6 μm	<8.88	–	–	–	–	–
J101542.92+425803.6	0.1973	43.27	24.68	C	12 μm	<2.15	–	–	–	–	–
J102053.67+483124.3*	0.0532	81.85	23.74	I	12 μm	2.54	0.05	6.51	124.8 ± 3.62	179.13 ± 11.06	−67.23 ± 4.92
J102400.53+511248.1	0.2139	47.12	24.8	C	dp	2.02	0.0759	17.72	179.18 ± 55.84	334.89 ± 60.66	−409.18 ± 22.06
J102544.22+102230.4	0.0457	92.83	23.66	C	dp	2.72	0.1222	9.62	66.95 ± 4.9	81.26 ± 6.18	−15.43 ± 6.68
J102838.69+170211.2	0.1691	47.54	24.58	I	dp	<3.66	–	–	–	–	–
J103053.58+411316.0	0.0921	41.12	23.94	C	dp	<1.85	–	–	–	–	–
J103214.01+275601.6	0.0852	29.82	23.73	I	4.6 μm	<1.46	–	–	–	–	–
J103653.01+444818.1	0.1274	32.52	24.14	C	12 μm	<2.71	–	–	–	–	–
J103719.33+433515.3*	0.0247	142.0	23.29	C	12 μm	<1.83	–	–	–	–	–
J103932.12+461205.3	0.1861	30.81	24.48	I	dp	2.78	0.0859	14.75	86.1 ± 9.25	127.26 ± 12.78	3.23 ± 6.0
J104029.94+295757.7*	0.0909	407.0	24.93	C	12 μm	<2.84	–	–	–	–	–
J104609.61+165511.4*	0.2069	63.21	24.89	C	4.6 μm	<2.42	–	–	–	–	–
J104643.83+315301.1	0.1166	38.35	24.13	C	dp	<3.72	–	–	–	–	–
J104801.21+151438.4	0.2161	46.28	24.8	I	12 μm	<2.51	–	–	–	–	–
J104931.69+232723.6	0.0631	81.23	23.89	I	dp	<1.72	–	–	–	–	–
J105327.25+205835.9*	0.0526	79.07	23.72	C	12 μm	1.96	0.023	2.59	156.05 ± 15.46	189.77 ± 20.9	−58.39 ± 6.85
J105731.17+405646.1	0.0251	31.74	22.66	C	dp	<2.66	–	–	–	–	–
J110017.98+100256.8	0.036	125.77	23.58	2.0	4.6 μm	2.87	0.2308	42.85	101.22 ± 11.9	166.2 ± 15.01	−15.04 ± 3.68
J110305.78+191702.2*	0.2143	98.95	25.12	C	dp	<2.35	–	–	–	–	–
J111113.19+284147.0	0.0287	36.42	22.84	C	12 μm	2.47	0.0927	18.3	180.98 ± 28.6	211.38 ± 31.87	54.73 ± 14.26
J111622.70+291508.2*	0.0453	72.88	23.54	C	dp	<1.8	–	–	–	–	–
J111834.85+614638.2	0.1924	38.52	24.61	C	dp	<2.58	–	–	–	–	–
J111836.00+313638.6	0.1185	52.89	24.29	I	dp	<2.72	–	–	–	–	–
J111916.54+623925.7	0.1102	32.28	24.0	C	12 μm	3.63	0.2688	31.63	95.62 ± 15.1	147.91 ± 18.15	−119.22 ± 12.38
J112030.04+273610.7*	0.1125	177.0	24.76	C	4.6 μm	4.39	0.147	10.93	62.48 ± 1.25	95.5 ± 3.63	−107.64 ± 2.03
J112156.70+431456.9	0.1854	37.72	24.56	C	12 μm	<2.54	–	–	–	–	–
J112332.04+235047.8	0.207	142.69	25.25	I	dp	3.75	0.1048	5.01	156.19 ± 13.68	184.03 ± 15.59	219.69 ± 17.29
J112349.91+201654.4*	0.1304	102.0	24.66	I	12 μm	<3.51	–	–	–	–	–
J113142.27+470008.6*	0.1257	99.6	24.62	I	dp	<2.65	–	–	–	–	–
J113230.99+573109.3	0.1804	36.73	24.53	C	dp	<2.68	–	–	–	–	–

Table A.1. continued.

Source J2000	z_{opt}	$S_{1.4\ GHz}$ [mJy]	$P_{1.4\ GHz}$ [W Hz^{-1}]	Radio type [C/E/I]	WISE type (6)	Noise (3σ) [mJy]	τ_{peak}	$\int \tau\, dv$ [km s^{-1}]	FWHM [km s^{-1}]	FW20 [km s^{-1}]	Centroid [km s^{-1}]
J113359.22+490343.4*	0.0316	168.0	23.59	I	dp	<1.84	–	–	–	–	–
J113446.55+485721.9	0.0316	44.62	23.01	I	dp	<2.25	–	–	–	–	–
J113903.77+262142.2	0.0223	41.6	22.67	C	4.6 μm	<2.26	–	–	–	–	–
J114505.01+193622.8*	0.0216	777.0	23.91	I	dp	<2.33	–	–	–	–	–
J114520.25+642623.4	0.0616	73.94	23.83	I	dp	<1.81	–	–	–	–	–
J114722.13+350107.5*	0.0629	276.0	24.42	I	12 μm	<1.65	–	–	–	–	–
J115531.39+545200.4	0.0496	51.46	23.48	C	dp	<1.78	–	–	–	–	–
J115742.64+330810.4	0.0803	39.1	23.79	C	12 μm	<1.7	–	–	–	–	–
J115954.66+302727.0	0.1064	23.44	23.83	C	12 μm	<2.54	–	–	–	–	–
J120231.12+163741.8*	0.1195	81.6	24.48	C	12 μm	3.42	0.042	7.27	174.98 ± 37.74	301.47 ± 50.03	−148.3 ± 31.29
J120255.33+261518.7	0.1936	36.39	24.59	C	4.6 μm	<1.52	–	–	–	–	–
J120303.50+603119.1*	0.0653	153.0	24.2	C	4.6 μm	<1.83	–	–	–	–	–
J120320.81+131934.3	0.0584	107.17	23.94	C	dp	<2.11	–	–	–	–	–
J120551.46+203119.0*	0.0238	80.0	23.01	C	12 μm	2.03	0.034	3.23	90.26 ± 8.7	122.3 ± 9.81	17.71 ± 3.45
J120805.55+251414.2	0.0225	50.66	22.77	C	dp	<1.84	–	–	–	–	–
J120855.60+464113.8*	0.101	68.38	24.25	I	12 μm	2.29	0.052	2.48	32.09 ± 0.81	68.99 ± 1.49	33.84 ± 1.1
J121030.47+310518.6	0.0577	26.62	23.33	C	dp	<1.12	–	–	–	–	–
J121329.27+504429.3*	0.0308	110.0	23.38	C	dp	<2.07	–	–	–	–	–
J121856.15+122643.0	0.0932	45.73	24.0	C	dp	<1.58	–	–	–	–	–
J122121.94+301037.2*	0.1836	60.0	24.76	C	4.6 μm	<2.58	–	–	–	–	–
J122513.09+321401.6	0.0592	50.84	23.63	C	dp	1.33	0.1493	10.49	54.51 ± 11.08	125.9 ± 13.92	168.95 ± 10.0
J122519.14+162104.6	0.197	28.33	24.5	C	dp	<2.92	–	–	–	–	–
J122622.51+640622.0	0.1102	47.1	24.17	I	dp	<3.18	–	–	–	–	–
J122823.09+162612.7*	0.23	116.92	25.26	I	12 μm	<2.66	–	–	–	–	–
J123011.85+470022.7*	0.0391	93.76	23.52	C	dp	<1.76	–	–	–	–	–
J123200.55+331747.6*	0.0788	93.83	24.16	I	4.6 μm	1.68	0.034	3.76	145.75 ± 7.25	174.74 ± 9.48	−49.83 ± 4.28
J123349.26+502622.7*	0.2068	135.0	25.22	I	4.6 μm	<2.01	–	–	–	–	–
J123905.13+174457.5	0.0654	66.4	23.84	I	dp	2.14	0.0477	2.72	78.49 ± 14.24	103.59 ± 15.73	40.05 ± 7.72
J124135.95+162033.6	0.0702	40.21	23.68	I	dp	<2.51	–	–	–	–	–
J124351.24+185025.9	0.228	30.19	24.67	I	dp	<1.89	–	–	–	–	–
J124428.54+331546.2	0.0843	71.48	24.1	I	dp	<1.99	–	–	–	–	–
J124707.32+490017.9*	0.2069	1140.0	26.15	C	4.6 μm	1.78	0.002	0.46	369.58 ± 82.31	586.32 ± 51.67	−284.84 ± 28.45
J124709.68+324705.0	0.1351	32.21	24.19	C	4.6 μm	<2.48	–	–	–	–	–
J125220.88+395100.9	0.2253	26.32	24.6	C	4.6 μm	<2.31	–	–	–	–	–
J125236.90+285150.7*	0.1951	430.0	25.67	I	12 μm	<2.14	–	–	–	–	–
J125431.43+262040.6	0.0691	36.76	23.63	I	dp	<2.2	–	–	–	–	–
J125433.26+185602.2*	0.1154	75.84	24.42	C	12 μm	5.71	0.068	5.0	60.1 ± 0.0	140.9 ± 0.0	356.29 ± 0.0
J130125.26+291849.5	0.0234	35.64	22.65	C	4.6 μm	1.52	0.0452	8.4	147.61 ± 21.97	217.78 ± 23.81	53.95 ± 12.0
J130132.61+463402.7*	0.2055	97.0	25.07	C	12 μm	2.01	0.018	4.24	172.41 ± 41.9	584.1 ± 85.29	−308.84 ± 40.27
J130346.59+191617.4*	0.0635	69.52	23.83	I	dp	<2.59	–	–	–	–	–
J130556.95+395621.5	0.1535	35.84	24.36	C	dp	4.08	0.0844	8.2	126.22 ± 23.11	141.49 ± 26.79	−18.96 ± 16.0
J130619.24+111339.7	0.0857	118.97	24.34	I	dp	<2.91	–	–	–	–	–
J130621.72+434751.2*	0.2026	136.54	25.21	I	dp	<2.84	–	–	–	–	–
J130837.91+434415.1*	0.0358	60.81	23.26	C	dp	<1.86	–	–	–	–	–
J131424.68+621945.8*	0.1308	72.0	24.51	I	dp	<2.96	–	–	–	–	–
J131535.10+620728.4	0.0308	44.72	22.99	2.0	4.6 μm	1.83	0.0575	10.52	283.09 ± 29.75	324.38 ± 30.35	142.39 ± 15.29

Table A.1. continued.

Source J2000	z_{opt}	$S_{1.4\ GHz}$ [mJy]	$P_{1.4\ GHz}$ [W Hz^{-1}]	Radio type [C/E/I]	WISE type (6)	Noise (3σ) [mJy]	τ_{peak}	$\int \tau\, dv$ [km s^{-1}]	FWHM [km s^{-1}]	FW20 [km s^{-1}]	Centroid [km s^{-1}]
J131739.20+411545.6*	0.0661	246.0	24.41	C	dp	1.69	0.031	4.79	133.97 ± 32.35	245.21 ± 75.52	59.19 ± 147.78
J131941.39+162852.5	0.1587	12.18	23.92	C	dp	<3.63	–	–	–	–	–
J132035.40+340821.7*	0.0231	96.6	23.07	2.0	4.6 μm	1.8	0.162	46.64	272.0 ± 4.29	416.47 ± 4.67	26.57 ± 1.94
J132513.37+395553.2*	0.0756	36.81	23.71	C	dp	1.75	0.053	9.46	138.16 ± 52.7	210.53 ± 80.31	−133.97 ± 20.58
J132524.03+492022.7	0.1867	35.89	24.55	C	12 μm	<3.72	–	–	–	–	–
J133455.94+134431.7	0.0231	26.31	22.5	C	dp	4.14	0.1544	15.68	130.14 ± 8.44	150.73 ± 18.68	−101.17 ± 14.06
J133817.24+481629.7	0.0276	79.28	23.14	2.0	4.6 μm	2.51	0.1014	7.26	139.61 ± 15.7	234.59 ± 23.93	176.44 ± 16.81
J134035.20+444817.3*	0.0654	36.22	23.57	2.0	4.6 μm	1.69	0.26	12.3	43.43 ± 8.54	62.65 ± 2.45	−23.25 ± 1.44
J134105.10+395945.4	0.1715	59.29	24.68	C	12 μm	<3.9	–	–	–	–	–
J134111.14+302241.3	0.0404	38.72	23.17	C	4.6 μm	1.98	0.0298	7.78	208.44 ± 25.28	242.09 ± 29.78	−2.42 ± 27.96
J134442.16+555313.5*	0.0373	132.0	23.63	2.0	4.6 μm	1.79	0.091	45.28	570.07 ± 2.12	638.38 ± 2.11	84.89 ± 0.08
J134620.46+130501.6	0.0811	46.57	23.88	C	12 μm	<2.11	–	–	–	–	–
J134649.45+142401.7	0.0216	162.0	23.23	C	4.6 μm	2.4	0.0367	4.15	248.73 ± 8.93	282.45 ± 11.18	36.82 ± 10.0
J134808.76+304908.9	0.1692	49.82	24.6	C	dp	<3.39	–	–	–	–	–
J134840.10+181716.1	0.0731	36.63	23.68	C	4.6 μm	<2.18	–	–	–	–	–
J135217.88+312646.4*	0.0452	3530.0	25.23	I	4.6 μm	2.48	0.057	45.28	99.94 ± 1.01	230.82 ± 0.41	−141.6 ± 0.18
J135314.08+374113.9	0.2159	32.59	24.65	C	dp	<3.15	–	–	–	–	–
J135646.10+102609.0	0.1231	61.02	24.38	C	4.6 μm	5.1	0.0614	10.41	128.68 ± 21.1	147.99 ± 25.04	169.32 ± 15.0
J135806.05+214021.1	0.0664	61.05	23.81	I	dp	2.09	0.1365	8.17	49.71 ± 7.51	72.34 ± 11.28	2.43 ± 3.0
J135908.74+280121.3	0.0645	34.06	23.53	C	dp	<2.33	–	–	–	–	–
J135942.61+124412.5	0.0392	44.4	23.2	I	dp	<1.79	–	–	–	–	–
J140026.40+175133.3*	0.0506	87.7	23.72	C	12 μm	<1.91	–	–	–	–	–
J140051.58+521606.5*	0.1179	176.0	24.8	C	12 μm	<3.66	–	–	–	–	–
J140810.47+524048.1*	0.0829	176.0	24.48	I	dp	<3.14	–	–	–	–	–
J140935.47+575841.2*	0.1799	114.0	25.01	C	12 μm	<3.92	–	–	–	–	–
J141134.14+294914.1	0.1861	12.36	24.08	C	dp	<2.01	–	–	–	–	–
J141149.43+524900.1*	0.0765	393.14	24.75	I	dp	<1.96	–	–	–	–	–
J141203.47+292801.7	0.1147	31.47	24.03	I	12 μm	<4.14	–	–	–	–	–
J141557.25+495334.6	0.1854	37.87	24.57	I	4.6 μm	<2.15	–	–	–	–	–
J141652.95+104826.7	0.0247	31.36	22.64	I	dp	<2.65	–	–	–	–	–
J142210.81+210554.1*	0.1915	84.3	24.94	C	dp	2.22	0.048	8.36	179.82 ± 14.28	274.93 ± 22.61	−196.05 ± 6.23
J142810.35+123711.7	0.0792	38.05	23.77	I	dp	<1.68	–	–	–	–	–
J142832.60+424021.0	0.1293	37.09	24.21	I	4.6 μm	<2.23	–	–	–	–	–
J143418.19+242444.2	0.085	47.45	23.93	C	dp	<1.62	–	–	–	–	–
J143521.67+505122.9*	0.0997	141.0	24.55	C	12 μm	2.04	0.013	3.55	285.61 ± 56.38	422.04 ± 52.61	−66.71 ± 24.9
J144104.37+532008.7	0.105	40.65	24.06	2.0	4.6 μm	<2.44	–	–	–	–	–
J144433.70+192121.5	0.1905	121.02	25.1	I	dp	<1.91	–	–	–	–	–
J144557.78+173828.6	0.0653	270.89	24.45	I	12 μm	<3.21	–	–	–	–	–
J144712.76+404744.9*	0.1951	348.0	25.58	I	4.6 μm	<2.08	–	–	–	–	–
J144921.58+631614.0*	0.0417	2500.0	25.01	I	12 μm	2.64	0.005	1.21	162.42 ± 9.77	460.94 ± 90.81	20.19 ± 14.2
J145049.40+100649.1	0.0545	48.22	23.53	C	dp	<1.96	–	–	–	–	–
J150034.56+364845.1*	0.0661	60.66	23.81	C	12 μm	2.11	0.19	20.3	100.97 ± 15.38	161.26 ± 54.0	17.96 ± 24.06
J150151.12+163705.9	0.1489	22.61	24.13	I	12 μm	<3.06	–	–	–	–	–
J150457.12+260058.4*	0.054	190.0	24.12	C	dp	<2.27	–	–	–	–	–
J150656.41+125048.6	0.0223	66.27	22.87	I	12 μm	<3.66	–	–	–	–	–
J150721.87+101844.8	0.078	403.28	24.78	C	12 μm	2.93	0.009	1.29	74.08 ± 7.24	241.14 ± 8.78	−16.73 ± 18.0

Table A.1. continued.

Source J2000	z_{opt}	$S_{1.4\ GHz}$ [mJy]	$P_{1.4\ GHz}$ [W Hz^{-1}]	Radio type [C/E/I]	WISE type (6)	Noise (3σ) [mJy]	τ_{peak}	$\int \tau\, dv$ [km s^{-1}]	FWHM [km s^{-1}]	FW20 [km s^{-1}]	Centroid [km s^{-1}]
J150950.99+155730.3*	0.1874	424.0	25.62	C	dp	<2.11	–	–	–	–	–
J151319.23+343133.7	0.1272	34.59	24.17	C	12 μm	3.12	0.2491	37.97	134.03 ± 22.93	180.45 ± 25.97	23.93 ± 9.76
J151641.59+291809.2*	0.1299	72.07	24.51	I	12 μm	<4.13	–	–	–	–	–
J151838.90+404500.2	0.0652	54.42	23.75	C	dp	<1.41	–	–	–	–	–
J152045.04+483922.9	0.078	47.01	23.85	I	dp	<1.54	–	–	–	–	–
J152115.79+151207.8*	0.2148	405.0	25.74	C	dp	<2.83	–	–	–	–	–
J152326.91+283732.5	0.0824	89.41	24.18	I	dp	<2.12	–	–	–	–	–
J152349.34+321350.2*	0.11	182.0	24.75	C	12 μm	<2.89	–	–	–	–	–
J152446.01+230723.5	0.2157	40.76	24.74	C	12 μm	1.95	0.0375	9.47	290.22 ± 26.32	376.95 ± 29.55	125.05 ± 16.0
J152500.83+332359.8*	0.0816	58.73	23.98	I	dp	<1.85	–	–	–	–	–
J152650.94+101320.8	0.2243	45.15	24.83	I	dp	<2.69	–	–	–	–	–
J152922.49+362142.2*	0.0989	37.8	23.97	C	12 μm	2.36	0.075	18.35	231.54 ± 31.63	360.19 ± 38.04	−29.27 ± 17.78
J153058.19+573625.2	0.1733	37.76	24.5	I	4.6 μm	<5.34	–	–	–	–	–
J153202.23+301628.9*	0.0653	32.94	23.53	C	12 μm	<2.04	–	–	–	–	–
J153437.61+251311.4	0.0339	43.39	23.06	C	12 μm	2.65	0.1317	10.92	40.88 ± 6.26	141.08 ± 8.11	−85.83 ± 7.0
J153452.95+290919.8	0.201	48.57	24.75	C	12 μm	1.72	0.0275	6.77	233.7 ± 31.87	320.14 ± 35.97	26.61 ± 27.04
J153535.08+134752.7	0.0524	25.47	23.22	C	12 μm	<2.57	–	–	–	–	–
J153901.66+353046.0*	0.0778	90.91	24.13	C	12 μm	<1.71	–	–	–	–	–
J153935.60+553015.9	0.0517	24.18	23.18	C	dp	<1.75	–	–	–	–	–
J154144.30+472754.8	0.1104	82.92	24.41	I	dp	<2.84	–	–	–	–	–
J154146.55+455614.3	0.2023	44.06	24.72	C	12 μm	<2.75	–	–	–	–	–
J154818.27+573549.3	0.0742	32.15	23.64	C	12 μm	<1.66	–	–	–	–	–
J154912.33+304716.4*	0.1116	914.0	25.47	I	12 μm	<3.65	–	–	–	–	–
J155343.59+234825.4*	0.1176	168.04	24.78	I	4.6 μm	<5.62	–	–	–	–	–
J155424.12+201125.4	0.2223	53.52	24.89	I	12 μm	<2.24	–	–	–	–	–
J155603.91+242652.8*	0.0425	92.13	23.59	I	dp	<1.91	–	–	–	–	–
J155611.61+281133.3*	0.2079	84.14	25.02	I	dp	<2.0	–	–	–	–	–
J155645.91+334248.9	0.2069	75.22	24.97	I	dp	<2.89	–	–	–	–	–
J155902.70+230830.4	0.1932	43.31	24.66	C	4.6 μm	2.2	0.0449	17.72	441.28 ± 22.82	520.07 ± 25.77	96.76 ± 18.4
J155953.90+423339.9	0.2169	44.2	24.78	C	dp	<1.72	–	–	–	–	–
J155953.98+444232.4*	0.0417	57.82	23.37	C	dp	<2.04	–	–	–	–	–
J160246.39+524358.3*	0.1057	577.0	25.22	C	12 μm	2.0	0.015	4.58	463.6 ± 29.76	673.64 ± 21.6	−255.51 ± 11.76
J160332.08+171155.3*	0.034	278.0	23.87	I	dp	2.26	0.066	3.5	46.98 ± 2.59	71.7 ± 2.85	−15.75 ± 1.25
J160338.06+155402.5*	0.1098	100.0	24.49	C	12 μm	3.04	0.125	5.11	357.8 ± 33.71	499.9 ± 7.26	−35.77 ± 3.28
J160426.51+174431.1*	0.0409	72.96	23.45	2.0	12 μm	<2.86	–	–	–	–	–
J160616.03+181459.8*	0.0369	225.0	23.85	I	dp	<2.24	–	–	–	–	–
J160821.14+282843.2*	0.0502	113.0	23.83	I	dp	<1.79	–	–	–	–	–
J160907.18+131908.2	0.1836	75.75	24.86	C	dp	<2.66	–	–	–	–	–
J160952.60+133148.0	0.0357	33.84	23.0	C	4.6 μm	4.08	0.1596	22.33	281.43 ± 26.2	308.18 ± 28.99	37.59 ± 30.15
J161114.11+265524.2	0.0319	69.49	23.21	I	dp	<2.66	–	–	–	–	–
J161217.62+282546.4*	0.0531	78.47	23.72	C	dp	2.58	0.061	5.0	77.16 ± 11.19	114.96 ± 12.2	−20.64 ± 4.55
J161419.62+502756.2*	0.0603	80.56	23.85	I	dp	<1.99	–	–	–	–	–
J161541.21+471111.7*	0.1986	134.55	25.18	I	4.6 μm	<3.06	–	–	–	–	–
J161740.53+350015.1	0.0298	141.18	23.46	I	dp	2.5	0.0376	1.55	113.76 ± 16.41	134.27 ± 17.37	−189.92 ± 9.48

Table A.1. continued.

Source J2000	z_{opt}	$S_{1.4\ GHz}$ [mJy]	$P_{1.4\ GHz}$ [W Hz^{-1}]	Radio type [C/E/I]	WISE type (6)	Noise (3σ) [mJy]	τ_{peak}	$\int \tau\, dv$ [km s^{-1}]	FWHM [km s^{-1}]	FW20 [km s^{-1}]	Centroid [km s^{-1}]
J162318.73+370547.5	0.2029	46.92	24.75	I	dp	<14.97	–	–	–	–	–
J162424.49+483142.3*	0.0571	67.42	23.72	C	dp	<1.99	–	–	–	–	–
J162839.03+252755.9	0.2199	63.49	24.96	I	12 μm	<2.39	–	–	–	–	–
J163124.69+250309.8	0.0623	39.31	23.56	C	dp	<2.27	–	–	–	–	–
J163804.02+264329.1	0.0652	40.64	23.62	C	dp	2.52	0.1196	13.6	110.78 ± 13.82	159.24 ± 15.02	95.88 ± 6.74
J163844.80+275439.1	0.1035	32.32	23.95	I	dp	3.54	0.1166	27.45	164.05 ± 15.64	280.29 ± 17.71	−478.5 ± 14.0
J163956.07+112757.4	0.0792	159.39	24.39	C	4.6 μm	4.98	0.1264	12.52	46.59 ± 6.99	68.09 ± 7.58	−36.04 ± 1.09
J164331.91+304835.5	0.184	46.69	24.65	C	4.6 μm	<3.9	–	–	–	–	–
J164332.24+254206.7	0.0571	54.43	23.63	I	dp	<2.69	–	–	–	–	–
J164419.97+454644.4	0.2246	89.39	25.12	C	12 μm	<1.82	–	–	–	–	–
J164516.33+132130.2	0.1934	78.15	24.92	I	12 μm	<3.57	–	–	–	–	–
J165240.83+231847.3	0.1623	53.8	24.59	I	dp	<3.15	–	–	–	–	–
J170528.99+221604.8	0.0496	62.65	23.56	I	dp	<1.24	–	–	–	–	–
J170727.45+260957.9	0.1125	42.74	24.14	C	dp	<1.86	–	–	–	–	–
J170735.95+353949.6	0.164	103.91	24.89	I	dp	<2.86	–	–	–	–	–
J170815.25+211117.7	0.2241	34.36	24.71	C	12 μm	2.92	0.1569	28.38	211.14 ± 17.49	284.89 ± 20.99	3.23 ± 13.0
J171056.30+394131.2	0.0622	77.57	23.86	I	dp	<1.8	–	–	–	–	–
J171522.97+572440.3	0.0273	45.84	22.89	C	dp	<2.1	–	–	–	–	–
J171523.73+302824.1	0.1111	30.66	23.99	C	dp	<2.56	–	–	–	–	–
J172223.65+320128.2	0.227	68.38	25.02	I	dp	<3.24	–	–	–	–	–